UNIVERSITY OF CALIFORNIA

Los Angeles

High Capacity Cathode Materials for Next Generation Energy Storage

A dissertation submitted in partial satisfaction of the

requirements for the degree Doctor of Philosophy

in Chemistry

by

Benjamin John Papandrea

2017

ABSTRACT OF THE DISSERTATION

High Capacity Cathode Materials for Next Generation Energy Storage

by

Benjamin John Papandrea

Doctor of Philosophy in Chemistry

University of California, Los Angeles, 2017

Professor Xiangfeng Duan, Chair

Energy storage devices are of increasing importance for applications in mobile electronics, hybrid electric vehicles, and can also play a critical role in renewable energy harvesting, conversion and storage. Since its commercial inception in the 1990's, the lithium-ion battery represents the dominant energy storage technology for mobile power supply today. However, the total capacity of lithium-ion batteries is largely limited by the theoretical capacities of the cathode materials such as $LiCoO_2$ (272 mAh g^{-1}), and $LiFePO_4$ (170 mAh g^{-1}), and cannot satisfy the increasing consumer demand, thus new cathode materials with higher capacities must be explored. Two of the most promising cathode materials with significantly larger theoretical capacities are sulfur (1675 mAh g^{-1}) and air, specifically the oxygen (3840 mAh g^{-1}). However, the usage of either of these cathodic materials is plagued with numerous issues that must be overcome before their commercialization. In the first part of my dissertation, we investigated the usage of a three-dimensional graphene membrane for a high energy density lithium-air (Li-Air)

battery in ambient condition. One of the issues with Li-Air batteries is the many side reaction that can occur during discharge in ambient condition, especially with water vapor. Using a hydrophobic tortuous three-dimensional graphene membrane we are able to inhibit the diffusion of water vapor and create a lithium-air battery that cycles over 2000 times with a capacity limited at 140 mAh g^{-1}, over 100 cycles with a capacity limited at 1425 mAh g^{-1}, and over 20 cycles at the high capacity of 5700 mAh g^{-1}. In the second part of my dissertation, we investigate the usage of a three-dimensional graphene aerogel to maximize the loading of sulfur to create a freestanding electrode with high capacity for a lithium-sulfur (Li-S) battery. We demonstrated that our three-dimensional graphene aerogel could sustain a loading of 95% by weight, and we achieved a capacity of 969 mAh g^{-1} normalized by the entire electrode with a 90% sulfur loading. In the third and final part of my dissertation, we investigate the usage of catalysts for both Li-Air, and Li-S batteries. We demonstrate how different noble metal configurations are optimal for Li-Air batteries, showcase how different metals effect the sulfur reduction reaction, and how both Pt and Mn increase the capacity of Li-S battery by interacting with the sulfur redox reactions intermediate species.

This dissertation of Benjamin John Papandrea is approved.

Richard B. Kaner

Yu Huang

Xiangfeng Duan, Chair

University of California, Los Angeles

2017

Dedicated to my parents, my brother Alexander,

my sister Christina, and all my family and friends for their

unwavering support and encouragement

TABLE OF CONTENTS

List of Figures

Acknowledgements

I would like to use this opportunity to express my gratitude to those who have helped me flourish and succeed throughout the journey of obtaining my Ph.D. First and foremost, I would like to greatly thank my advisor, Professor Xiangfeng Duan, for his help, guidance and mentorship throughout the entirety of my Ph.D. Since I joined the group in the summer of 2012, he was there to provide insight, scientific discussion, and encouragement into the many different projects that I participated in. Due to his help, I was able to grow from a first year graduate student that was unsure of what I was doing, or really how to conduct research, to a fully fledged independent researcher whom is able to take ideas, forge my own hypothesis, carry out the necessary experiments, and understand and comprehend the results. Second, I would like to thank my committee members, Professor Yu Huang, Professor Richard B. Kaner, and Professor William Gelbart.

During the duration of my Ph.D, there were numerous graduate students and post docs that greatly contributed to my success that I would like to thank. First of all, I'd like to thank Dr. Anxiang Yin. He was my mentor during the first year of my Ph.D, and introduced me many different concepts, and analytical techniques. Second, I'd like to thank Dr. Xing Zhong for introducing me to battery research, and establishing the path I would take during my Ph.D. Third, Dr. Xu Xu for all the work we did together on many different projects, and Dr. Huilong Fei for his insights into electrochemistry and catalysis. Finally, I'd like to thank all the other member of my research group whom made the long journey to achieve my Ph.D an enjoyable experience.

VITA

2008	High School Diploma Santa Margarita Catholic High School Rancho Santa Margarita, CA
2012	Bachelor of Physical Science, Chemistry Bachelor of Music, Piano Performance University of California, Irvine Irvine, CA
2014	Master of Science in Chemistry University of California, Los Angeles Los Angeles, CA
Expected in 2017	Doctor of Philosophy in Chemistry University of California, Los Angles Los Angeles, CA

Chapter 1: High capacity energy storage cathode materials

1.1 Cathode materials

Energy storage devices are of increasing importance for applications in mobile electronics, hybrid electric vehicles, and can also play a critical role in renewable energy harvesting, conversion and storage. The lithium-ion battery represents the dominant energy storage technology for mobile power supplies today. Lithium-ion batteries function by Li-ions moving from the negative electrode (anode) to the positive (cathode) when discharging, and back when recharging. Not all materials can store the same amount of lithium, however, meaning different materials have different inherent capacities. The general formula for determining how much capacity material possesses is the following:

$$C_t = \frac{nF}{3600 \, X \, M}$$

In this formula, C_t represents the Specific Capacity (mAh g^{-1}) of a given material, n is the number of electrons produced when reacted with lithium, F is Faradays Constant, and M is the molecular weight of the material. Using this formula one is able to calculate the theoretical capacity of a material, for example, graphite's theoretical capacity is 372 mAh g^{-1} (where graphite's fully lithiated form is LiC_6), and silicon's theoretical capacity is 4211 mAh g^{-1} (where silicon fully lithiated form is $Li_{22}Si_5$). One might assume based on this that the battery with the highest capacity would be just simple taking the two materials with the two highest capacities and using them together in a cell, however, not all materials can act as an anode or a cathode. To determine whether a material is best for used for an anode or cathode, the potential of the

materials vs. Li must be investigated. In order to maximize the voltage of the cell, the anode reduction potential vs. Li must be as low as possible, and the reduction potential of the cathode must be as high as possible. This can be seen in the following formula:

$$E_{cell} = E_{red,cathode} - E_{red,anode}$$

E_{Cell} is the cell potential, and $E_{red,cathode}$ and $E_{red,\ anode}$ are the reduction potential vs Li of both the cathode and anode respectively. Generally, if a material possesses a reduction potential of less than 1.5 V vs. Li, then the material is considered an anodic material, and if the reduction potential of a material is greater than 1.5, it is considered a cathodic material. Based on the previous two equations, we are able to easily sort and separate materials based on both their capacity and whether the material is anodic or cathodic.

Today, the total capacity of lithium-ion batteries is largely limited by the theoretical capacities of the cathode materials such as $LiCoO_2$ (272 mAh g^{-1}), and $LiFePO_4$ (170 mAh g^{-1}), which is beginning fall short of increasing consumer demand.[1-4] Thus exploring cathode materials that provide a higher capacity such as oxygen (3842 mAh g^{-1}) using a lithium-air battery, or sulfur (1675 mAh g^{-1}) using a lithium-sulfur battery will pave the way for the next generation of energy storage.

1.2 Lithium-air batteries

Lithium-air batteries are known for their ultra high theoretical specific capacity of 3842 mAh g^{-1}. The general structure of a lithium-air batteries is seen in Figure 1.1,[5] where there is a pure lithium metal anode, an aqueous or non-aqueous electrolyte, followed by a porous carbon

cathode in which air is able to permeate though. Unlike a lithium-ion battery, no intercalation reaction occurs in a lithium-air battery, instead, two concerted reactions occur creating a product. During discharge, oxygen is reduced in the cathode and reacts with lithium ions produced from the anode to produce Li_2O_2. During recharge, the oxygen evolution reaction occurs and Li_2O_2 breaks down producing O_2 and Li^+.[7] Although the lithium-air batteries exhibits a high capacity, it is plagued with a number of serious issues.

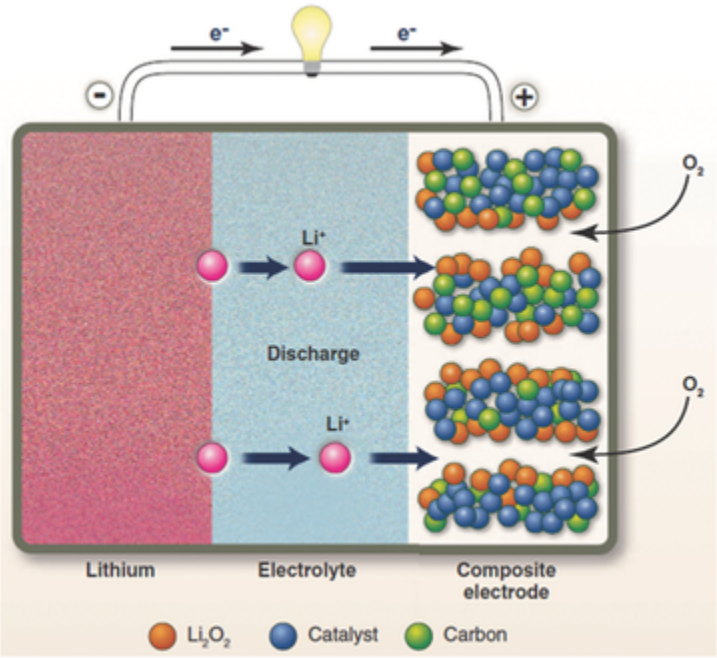

Figure 1.1. Design of lithium-air battery using a pure lithium anode, an electrolyte, and a porous carbon based cathode, usually with a catalyst to increase the kinetics of the oxygen reduction and oxygen evolution reactions.[5]

One of the most prominent issues with lithium-air batteries is the numerous reactions lithium can undergo when exposed to ambient air. Side reactions within the cathode cause severe capacity loss as well as cycle degradation. Ambient air is comprised of N_2 (78%), O_2 (21%), CO_2 (0.03%), and other gasses in trace quantities. There is also moisture content in air that varies with humidity. The reactions in ambient air that are possible within a lithium-air cell are the following:[5]

(1) $2Li + O_2 \leftrightarrow Li_2O_2$

(2) $4Li + O_2 \rightarrow 2Li_2O$

(3) $4Li + O_2 + 2H_2O \rightarrow 4LiOH$

(4) $4Li + O_2 + 2CO_2 \rightarrow 2Li_2CO_3$

(5) $2Li + 2H_2O \rightarrow LiOH + H_2$

(6) $2LiOH + CO_2 \rightarrow Li_2CO_3 + H_2O$

(7) $LiOH + H_2O \rightarrow LiOH\ H_2O$

(8) $2Li_2O_2 + 2CO_2 \rightarrow 2Li_2CO_3 + O_2$

(9) $2Li_2O_2 + 2H_2O \rightarrow 4LiOH + O_2$

Possible reactions with N_2 are ignored, as it is believed that N_2 does not react in the air cathode. Any that occurs in the cathode that cannot be fully reversed is considered a loss of capacity, and detrimental to the cell, thus targeting only reaction (1) is key to not losing capacity over many cycles. To combat this specifically designed catalysts can be used to kinetically enhance the reaction to Li_2O_2. For example, Dawei Su *et al.* have investigated a Pt_xCo_y alloy that demonstrates a capacity of 3100 mAh g^{-1} with the catalyst compared to only 600 mAh g-1 without it, which also has better cycleablity.[6]

Other than the many side reactions that can occur within a lithium-air battery, there are numerous other issues that need to be addressed prior to the commercialization of the lithium-air battery. First, the during cycling there is decomposition of the electrolyte due to the super oxide radicals (O_2^-) generated during cell operation.[7] Other electrolytes based on ethers and sulfones have been used, however, none show complete stability. Second, the growth of Li dendrites on the Li-metal anode due to the repeated Li dissolution/deposition process is also an

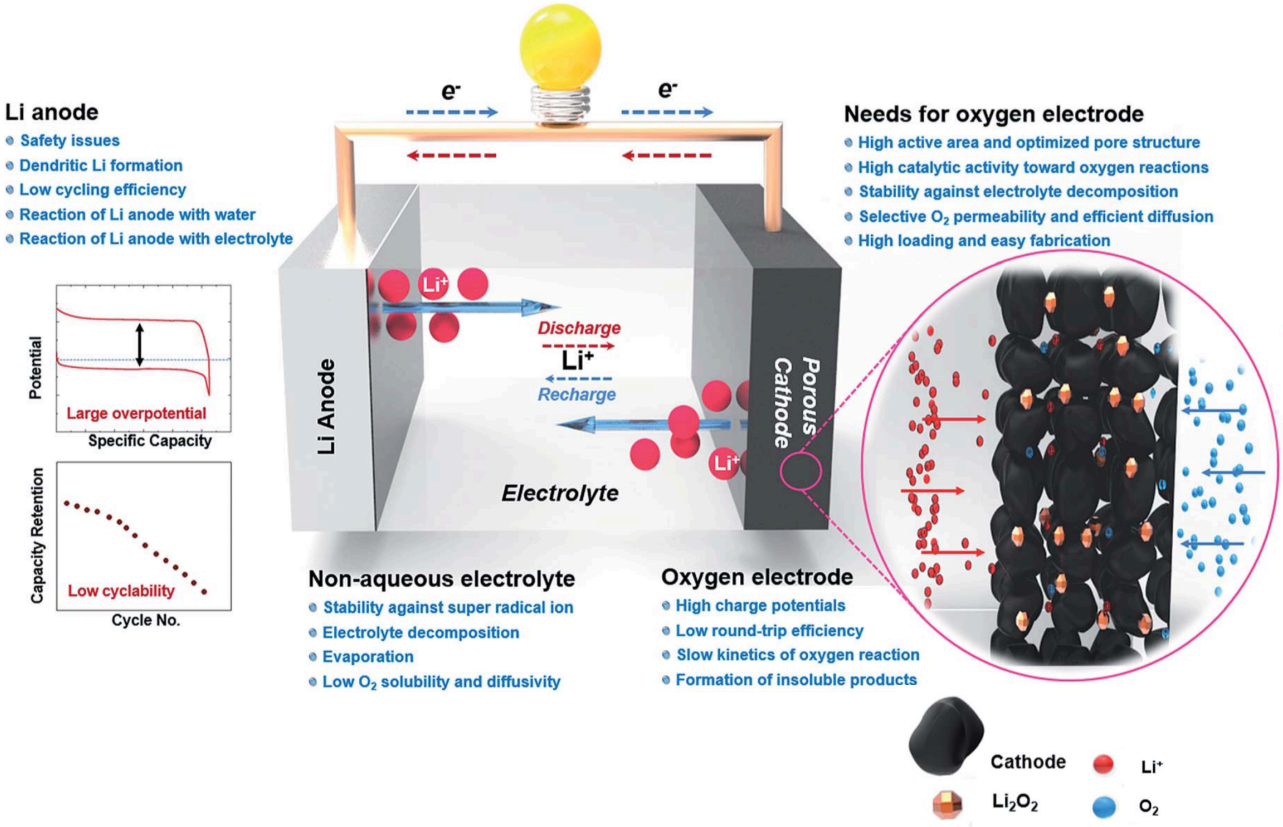

Figure 1.2. The technical overview of the challenges of lithium-air batteries.[7]

issue that can cause severe shorts within the cell. It is also very important to make sure Li does not react with undesirables such as a H_2O or the electrolyte. Third, both the oxygen reduction reaction (ORR) and oxygen evolution reaction (OER), which occur when discharging recharging respectively, have slow reaction kinetics. This limits the overall power density of the cell. Finally, during cycling there is cathode degradation. Build up of side reaction products can clog the pores of the cathode making oxygen diffusion significantly more difficult. An overview of the challenges and some solutions to all these problems can be seen in Figure 1.2.[7]

1.3 Lithium-sulfur Batteries

Lithium-sulfur (Li-S) batteries represent the next generation of battery technology, with the sulfur cathode offering a far higher theoretical capacity over Li-ion of 1675 mAh g^{-1}.[8-11] Furthermore, lithium-sulfur batteries have the ability to exceed both the power and energy density of today's energy storage devices as seen in the Ragone plot in Figure 1.3a.[12] However, there are many challenges associated with Li-S battery technology today, including the intrinsic insulating properties of sulfur and Li_2S, cathode degradation caused by volume expansion/contraction during discharge/recharge process, and the polysulfide shuttling effect.[13-19]

The intrinsic insulating properties of lithium-sulfur batteries are due to the high resistivity of both the starting active material, elemental sulfur, and the final discharge product Li_2S. Due to this high resistivity, a highly conductive supporting scaffold material must be used for cathode. The most commonly used are activated carbons, or graphene.[9-11] However, even when using these conductive materials in conjunction with sulfur it is difficult to achieve high rate capability due to both poor reaction kinetics and the other two issues.

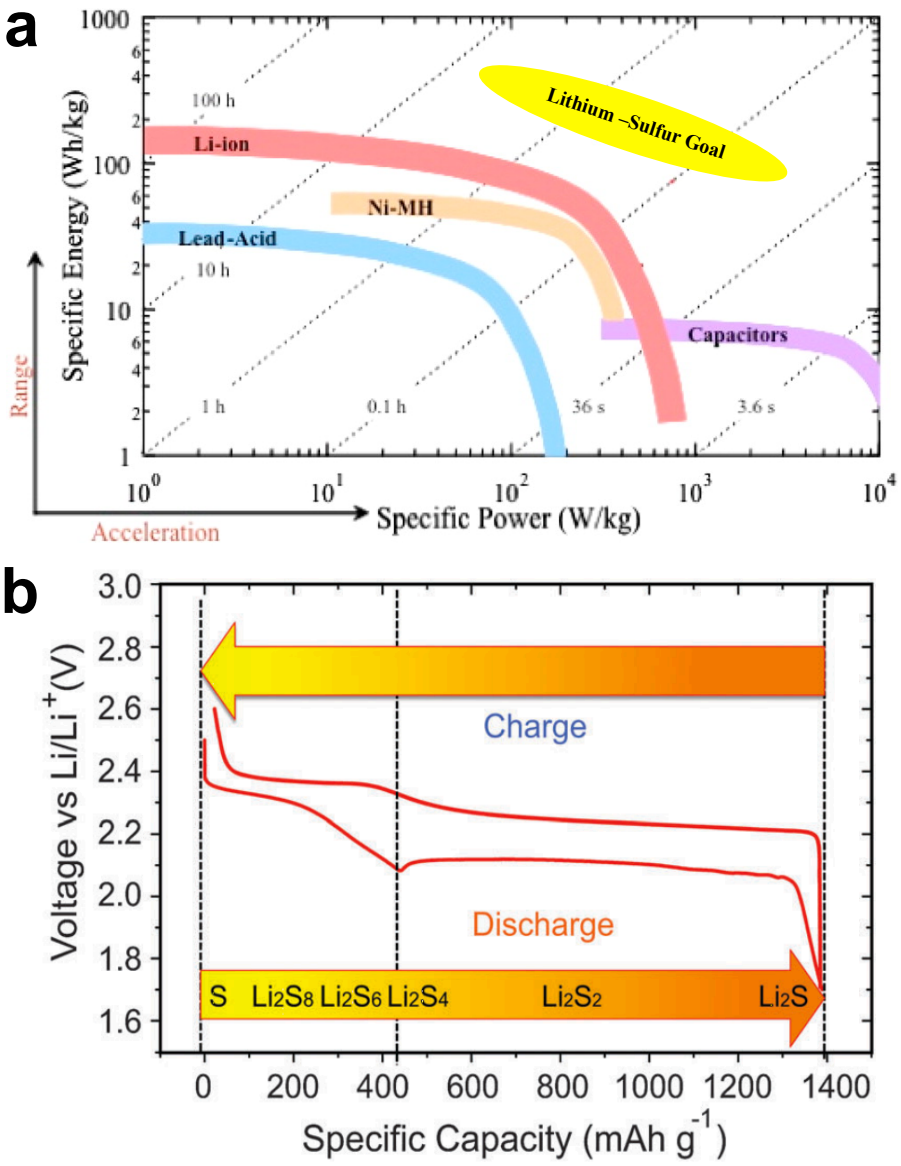

Figure 1.3. (a) Ragone plot detailing typical energy density and power density of todays energy storage devices vs. the goal of lithium-sulfur batteries. (b) Typical discharge/recharge curve of lithium-sulfur battery depicting the formation of different polysulfides.[9]

The second issue with lithium-sulfur batteries is the volume expansion of sulfur on discharge. Unlike lithium-ion batteries that undergo intercalation during charge and discharge with little volume change, lithium-sulfur batteries undergo a series of chemical reaction with a rather large volume change. As seen in Figure 1.3b,[9] during discharge, sulfur reacts with lithium to form a series of polysulfides, Li_2S_8, Li_2S_6, Li_2S_4, Li_2S_3, and Li_2S_2, before reaching the final discharge product Li_2S. Starting from cyclic octatomic sulfur, S_8, to the final discharge product, Li_2S, there is a volume expansion of 80%.[9] Volume expansion and contraction is detrimental to electrodes due to the fact that it may fragment the electrode material and break the connection with the current collector. In order to combat the volume expansion of sulfur, three-dimensional graphene or porous activated carbon have been used as flexible and/or porous conductive support/matrix for sulfur.[9]

Although the insulating nature and volume expansion of sulfur present a challenge, the largest issue with lithium-sulfur batteries is the polysulfide shuttling effect. As discussed previously, there are many different intermediates formed during the discharge and recharge reaction within the cell. Of those intermediates, Li_2S_8, Li_2S_6, Li_2S_4, Li_2S_3, are all soluble within the electrolyte of the lithium-sulfur battery. This is harmful to cell performance in two regards. First, during both charge and discharge lithium polysulfides dissolved in the electrolyte are able diffuse across the separator from the cathode to the anode and undergo a parasitic reaction with the anode producing an insulating layer, ruining the cell. Secondly, due to the fact that these polysulfides are able to escape from the cathode, there will be a continuing loss of active material with the continued operation of the battery[9] leading poor cycling performance. A schematic of polysulfide shuttling can be seen in Figure 1.4.[20]

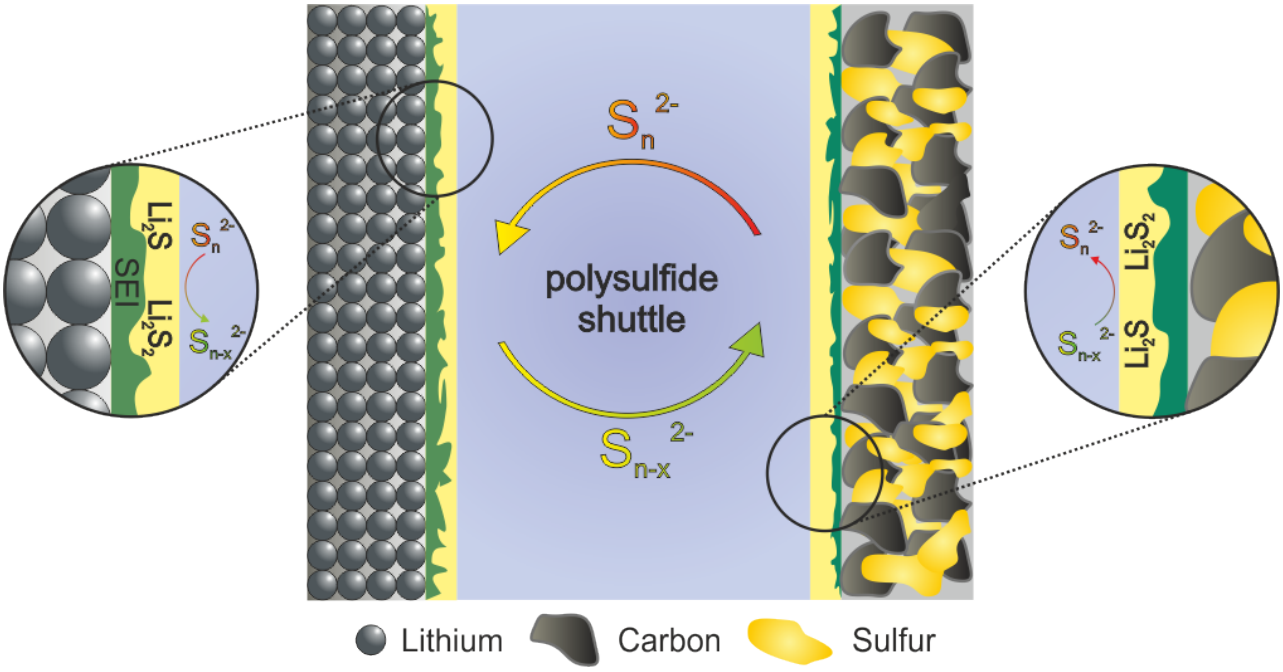

Figure 1.4. Schematic of polysulfide shuttling. The polysulfide intermediates are able to travel freely throughout the separator and deposit on both sides of the cell. This causes severe capacity loss.[20]

Many different approaches have been explored to inhibit the polysulfide shuttling effect. One method investigated is physical encapsulation of sulfur while still allowing lithium ions to penetrate. The physical encapsulation layer would trap the polysulfide within, inhibiting their diffusion into the electrolyte. Seh *et al.* encapsulated sulfur within a TiO_2 shell and demonstrated 1000 cycles with a capacity of 800 mAh g^{-1} at 0.5 C.[21] Another method is using the partial charges created by the lithium on the polysulfides to interact electrostatically with other metals that also have a partial charge. For example, Pang et al. used the conductive metal oxide Ti_4O_7 to

electrostatically bind to the lithium polysulfides, inhibiting their diffusion and increasing the cell cyclability.[22] Another method utilizes an extra layer of material between the cathode and the separator. Su et al. synthesized a functionalized carbon interlayer and placed it in between the cathode and separator when making the cell. The functional groups on the carbon interacted with the polysulfides resulting in a cell with high cycle life.[23] These methods constitute only some of the many ways to inhibit polysulfide shuttling.

1.4 References

1. Mizushima, K.; Jones, P.; Wiseman, P.; Goodenough, J. B. LixCoO2 (0<x≤1): a new cathode material for batteries of high energy density. *Mater. Res. Bull.* **1980**, 15, 783-789.
2. Yamada, A.; Chung, S.-C.; Hinokuma, K. Optimized LiFePO4 for lithium battery cathodes. *J. Electrochem. Soc.* **2001**, 148, A224-A229.
3. Armand, M.; Tarascon, J.-M. Building better batteries. *Nature* **2008**, 451, 652-657.
4. Tarascon, J.-M.; Armand, M. Issues and challenges facing rechargeable lithium batteries. *Nature* **2001**, 414, 359-367.
5. Geng, D., Ding, N., Hor, A., Chein, S., Liu, Z., Wuu, D., Sun, X., Zong, Y. From Lithium-Oxygen to Lithium-Air Batteries: Challenges and Opportunities. *Adv. Energy Mater.* **2016**, 6, 1502164.
6. Su, D., Kim, H.S., Kim, W.S., Wang, G. A study of Pt_xCo_y alloy nanoparticles as cathode catalysts for lithium-air batteries with improved catalytic activity. *J. of Power Sources*, **2013**, 244, 488-493.

7. Jung, K.N., Kim, J., Yamauchi, Y., Park, M.S., Lee, J.W., Kim, J.H. Rechargeable lithium–air batteries: a perspective on the development of oxygen electrodes. *J. Mater. Chem. A.* **2016**, 4, 14050.

8. Bruce, P. G.; Freunberger, S. A.; Hardwick, L. J.; Tarascon, J.-M. Li-O2 and Li-S batteries with high energy storage. *Nat. Mater*. **2012**, 11, 19-29.

9. Yang, Y.; Zheng, G.; Cui, Y. Nanostructured sulfur cathodes. *Chem. Soc. Rev*. **2013**, 42, 3018-3032.

10. Ji, X.; Lee, K. T.; Nazar, L. F. A highly ordered nanostructured carbon-sulphur cathode for lithium-sulphur batteries. *Nat. Mater.* **2009**, 8, 500-506.

11. He, G.; Ji, X.; Nazar, L. High "C" rate Li-S cathodes: sulfur imbibed bimodal porous carbons. *Energy Environ. Sci.* **2011**, 4, 2878-2883.

12. Expanding the Ragone Plot: Pushing the limits of Energy Storage. *J. Phys. Chem. Lett*. **2015**, 6, 3592−3593

13. Lin, T.; Tang, Y.; Wang, Y.; Bi, H.; Liu, Z.; Huang, F.; Xie, X.; Jiang, M. Scotch-tape-like exfoliation of graphite assisted with elemental sulfur and graphene–sulfur composites for high-performance lithium-sulfur batteries. *Energy Environ. Sci*. **2013**, 6, 1283-1290.

14. Manthiram, A.; Fu, Y.; Chung, S.-H.; Zu, C.; Su, Y.-S. Rechargeable lithium-sulfur batteries. Chem. Rev. **2014**, 114, 11751-11787.

15. Zhang, S. S. Liquid electrolyte lithium/sulfur battery: fundamental chemistry, problems, and solutions. *J. Power Sources* **2013**, 231, 153-162.

16. Ji, X.; Nazar, L. F. Advances in Li-S batteries. *J. Mater. Chem.* **2010**, 20, 9821-9826.

17. Zang, J.; An, T.; Dong, Y.; Fang, X.; Zheng, M.; Dong, Q.; Zheng, N. Hollow-in-hollow carbon spheres with hollow foam-like cores for lithium-sulfur batteries. *Nano Res*. **2015**, 8, 2663-2675.

18. Zhang, K.; Zhao, Q.; Tao, Z.; Chen, J. Composite of sulfur impregnated in porous hollow carbon spheres as the cathode of Li-S batteries with high performance. *Nano Res.* **2013**, 6, 38-46.

19. Qiu, Y.; Li, W.; Li, G.; Hou, Y.; Zhou, L.; Li, H.; Liu, M.; Ye, F.; Yang, X.; Zhang, Y. Polyaniline-modified cetyltrimethylammonium bromide-graphene oxide-sulfur nanocomposites with enhanced performance for lithium-sulfur batteries. *Nano Res.* **2014**, 7, 1355-1363.

20. Manthiram, A., Fu, Y., Su, Y.S. Challenges and Prospects of Lithium–Sulfur Batteries. *Accounts of Chemical Research.* **2013**, 5, 1125-1134.

21. Seh, Z.; Li, W.; Cha, J.; Zheng, G.; Yang, Y.; McDowell, M.; Hsu, P.; Cui, Y. Sulfur-TiO2 yolk-shell nanoacheticture with internal void space for long-cycle lithium-sulfur batteries. *Nature Comm*. **2013**, 4, 1331.

22. Pang, Q.; Kundu, D.; Cuisinier, M.; Nazar, L.F. Surface-enhanced redox chemistry of polysulfides on a metallic and polar host for lithium-sulfur batteries. *Nature Comm*. **2014**, 5,4759.

23. Su, Y.S., Manthiram, A. Lithium–sulphur batteries with a microporous carbon paper as a bifunctional interlayer. *Nature Comm*. **2012**. 3, 1116.

Chapter 2

2.1 Introduction

Lithium-air (Li-air) batteries with aprotic electrolytes have garnered intensive interest for mobile energy supplies because of its potential to offer an energy density far exceeding that of lithium-ion batteries and other energy storage systems.[1-8] Despite this exciting potential, the practical implementation of Li-air batteries is of considerable challenge, particularly with the electrolyte and air cathodes.[9-23] Cathode materials such as nanoporous metal oxides,[24] gold,[25] TiC,[26] and carbon nanotubes[27] have been explored for optimizing the battery capacity and cycle life. Most studies to date have been focusing on Li-air batteries operation under pure oxygen conditions. However, the operation of Li-air batteries under ambient conditions is more relevant for practical applications and is considerably more challenging. The Maxpower group has shown that Li-air batteries operate significantly different in ambient conditions from that in a pure oxygen environment.[28-29] The low oxygen partial pressure in air can limit O_2 accessibility to the cathode. Thus, it is desirable to have a cathode electrode that is highly porous for fast oxygen diffusion and also with a high specific surface area for efficient charge/discharge cycles. Additionally, the water moisture in ambient air can react with the discharge product (Li_2O_2) and/or even corrode the Li anode to sabotage the inner systems of the battery and severely undermine the battery stability and cycling endurance.[30-32] A Li-air battery with a cathode composed of SWNTs and ionic liquid in gel has been reported with 100 cycles under ambient conditions[33] which however requires a high charge over-potential (charge voltage > 5 V) because of formation of undesired discharge product ($LiOH/Li_2CO_3$) without moisture protection.[34]

Graphene, a single atomic layer of graphite sheet, has been recently explored as Li-air battery electrode due to its excellent electrical conductivity and high surface area.[35-47]

Additionally, it has been suggested that the defects and functional groups on the reduced graphene oxide can function as catalytic active sites for both oxygen evolution reaction (OER) and oxygen reduction reaction (ORR) that are essential for the charge/discharge processes.[48-52] Yoo reported graphene sheets as air electrodes with a hybrid electrolyte, and demonstrated that the sp^3 bonding from edge and defect sites showed considerable catalytic activity in reducing and evolving oxygen.[48] Wang proposed a hierarchically porous carbon cathode, and reached stable primary discharge performance (11,060 mAh g^{-1}) under oxygen, but with limited cycle life (~2000 mAh g^{-1} for 10 cycles) in secondary performance.[50] Ren reported a 3D hierarchical porous graphene aerogel with tunable meso-pores and cycled over 100 times at ~1000 mAh g^{-1}, however did not delve into the structure performance in ambient conditions.[40] Moreover, binders such as polyvinylidene fluoride (PVDF) were generally used in cathode but found to be chemically reactive with discharge product (e.g. LiO_2, Li_2O_2, LiOH) and thus degrading the cycling performance.[53-55]

Here we propose a binder-free hydrophobic and densely packed three-dimensional (3D) graphene membrane as an effective cathode for the stable and reversible operation of Li-air batteries under ambient conditions. We demonstrate that the 3D graphene membrane allows for efficient transport of charges, electrolyte ions and oxygen, and high capacity storage of insulating discharge product, thus enabling a Li-air battery with exceptional performance, including a highest cycling capacity > 5700 mAh g^{-1} (up to 20 cycles) and excellent cycling behaviour (>2000 cycles at 140 mAh g^{-1} and >100 cycles at 1400 mAh g^{-1}), with a lifespan capacity of 100,000-300,000 mAh g^{-1}, comparable to that of lithium-ion battery cathode.

2.2 Experimental

Graphene oxide (GO) was prepared using modified Hummer's method [37-38]. Briefly, graphite (3.0 g) was added to concentrated sulfuric acid (70 mL) under stirring at room temperature; then sodium nitrate (1.5 g) was added, and the mixture was cooled to 0 ^{o}C. Under vigorous agitation, potassium permanganate (9.0 g) was added slowly to keep the temperature of the suspension lower than 20 ^{o}C. Successively, the reaction system was transferred to a 35－40 ^{o}C water bath for about 0.5 h, forming a thick paste. Then, 140 mL of water was added, and the solution was stirred for another 15 min. An additional 500 mL of water was added followed by a slow addition of 20 mL of H_2O_2 (30%), turning the color of the solution from brown to yellow. The mixture was filtered and washed with 1:10 HCl aqueous solution (250 mL) to remove metal ions followed by repeated washing with water and centrifugation to remove the acid. The resulting solid was dispersed in water by ultrasonication for 1 h to make a concentrated GO solution (~8.0 g/L). The solution then was uniformly coated onto the carbon paper, and freeze-dried to obtain a 3D porous GO membrane. Note that size of GO is controlled in the level of ~ 1 μm. Small pieces of GO will not be able create such a highly dense 3D graphene structure. The GO was reduced to graphene by annealing in an argon atmosphere at 400 ^{o}C. The resulting graphene membrane on carbon paper was then compressed and cut into round disks to create air-cathode electrodes for coin cells.

All the cells were assembled in an argon-filled glove box with water and oxygen content kept both below 0.1 ppm. The positive top cover was machine-drilled to create holes to enable gas diffusion. The cell consists of a metallic Li foil anode and the aforementioned graphene cathode with a commercial carbon paper as the current collector. A Celgard separator is used to

separate the cathode from the anode. A solution of 1 M solution of lithium nitrate ($LiNO_3$) in N,N-dimethylacetamide (DMA) was used as the electrolyte.

For the test in pure oxygen, the as prepared Li-air cell was kept in a homemade glass chamber flooded with oxygen during testing. For operation in ambient conditions, the as prepared Li-air cell was directly tested in the ambient air. Galvanostatic discharge/charge was performed with Maccor 4340.

For SEM and XRD analysis, Scanning electron microscopy (SEM JEOL 6700) was used to observe the morphology of the air cathode. X-ray Diffraction (XRD) pattern was carried out using Bruker D8 Discover Powder X-ray Diffractometer.

For the oxygen and moisture diffusion test, the dense graphene membrane was prepared on a copper foil with ~0.5 mm hole in diameter, with the compressed graphene membrane fully covering the hole. A closed homemade chamber with oxygen/moisture sensor inside and the graphene membrane covered copper foil seal was assembled in the glove box. After exposing to ambient air, the change of oxygen/moisture inside the chamber was recorded as a function of time.

2.3 Results and Discussion

The 3D graphene membrane exhibits several unique characteristics, making it an excellent air cathode material (Figure 2.1). First, the 3D graphene membrane consists of a highly conjugated and interlocked 3D network structure of graphene sheets, and is mechanically strong by itself as a binder-free air-cathode, preventing the associated structural/chemical instability and reducing the mass of passive components. Second, the highly interconnected 3D graphene network structure can ensure excellent electron transport properties across the entire network.

Third, the highly porous network of channels within the 3D graphene membrane can offer highly efficient diffusion pathways for oxygen and electrolyte ions. Moreover, the high specific surface area of porous graphene network with abundant defects can offer bountiful active sites for ORR

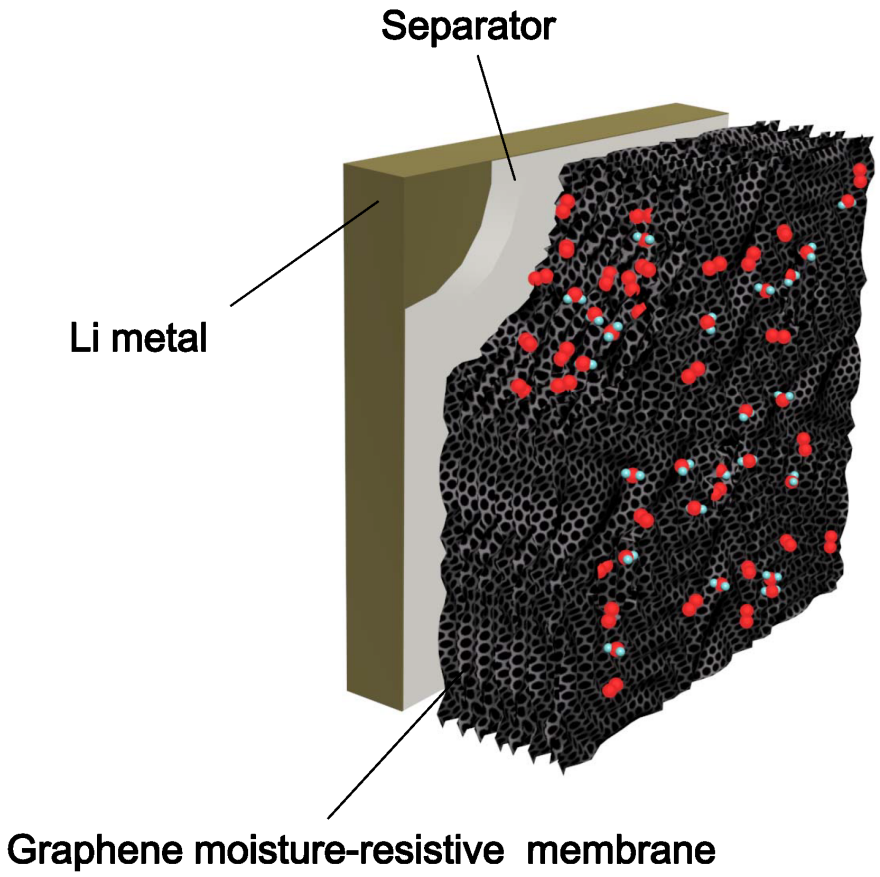

Figure 2.1. A schematic illustration of a Li-air battery with a Li metal anode, separator and 3D graphene moisture-resistive membrane cathode.

and OER for efficient charge/discharge processes. The 3D graphene skeleton structure can also allow high capacity deposition of the insulating discharge product Li_2O_2 while maintaining the overall structural and electronic integrity and stability under deep discharge state. Lastly, The highly tortuous, hydrophobic densely packed architecture can offer important O_2/H_2O selectivity

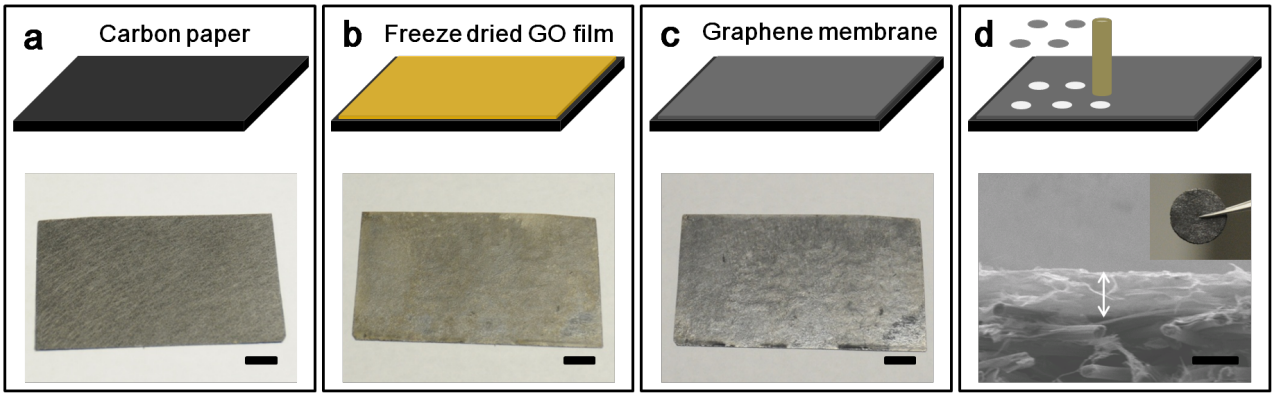

Figure 2.2. An illustration of the scalable preparation of the 3D graphene membrane cathode. (a) Commercial carbon paper is used as the support. (b) Graphene oxide is coated on the carbon paper. (c) Graphene membrane is formed after annealing. (d) Membrane is cut into round shaped disks for coin cell assembly and cross sectional SEM image of graphene membrane cathode. Scale bars are 1 cm in a,b,c, and 20 µm in d.

to ensure efficient oxygen diffusion while retarding the moisture ingression, minimizing the adverse impact of moisture under ambient conditions. Together, these unique attributes of the proposed graphene membrane cathode can enable a high capacity Li-air battery with stable cycling performance in both oxygen and ambient conditions.

A commercially available carbon paper was used as the support for the 3D graphene membrane cathode (Figure 2.2a). Figure 2.2d shows a typical scanning electron microscope (SEM) image of the as-prepared graphene thin membrane on the carbon paper. The thickness and the density of the graphene membrane can be readily tuned for various stability, energy and power requirements.

The coin cells assembled with 3D graphene membrane air cathode were first characterized by a galvanostatic discharge/charge process in pure oxygen (black curve in Figure 2.3a). The discharge voltage for the graphene membrane cathode is 2.71 V while the charging process shows a flat platform around 3.54 V. A similar test conducted under ambient conditions demonstrates a highly similar behavior with only a slight decrease in discharge voltage (2.67 V) and slight increase in charge voltage (3.59 V) (red curve in Figure 2.3a). We have further conducted multiple charge/discharge cycles in both oxygen and ambient conditions to evaluate the cycling endurance of the graphene membrane cathode. As a control experiment, we first tested a carbon black based air cathode, which exhibits expected performance in oxygen with little charge polarization (black curve in Figure 2.3b top), consistent with the previous report.[11] However, when operating under ambient conditions (red curve in Figure 2.3b top), significant voltage polarization is observed within the first few cycles and with the charge voltage quickly climbing up to 4.2 V where the electrolyte N,N-dimethylacetamide (DMA) could undergo irreversible decomposition.[11]

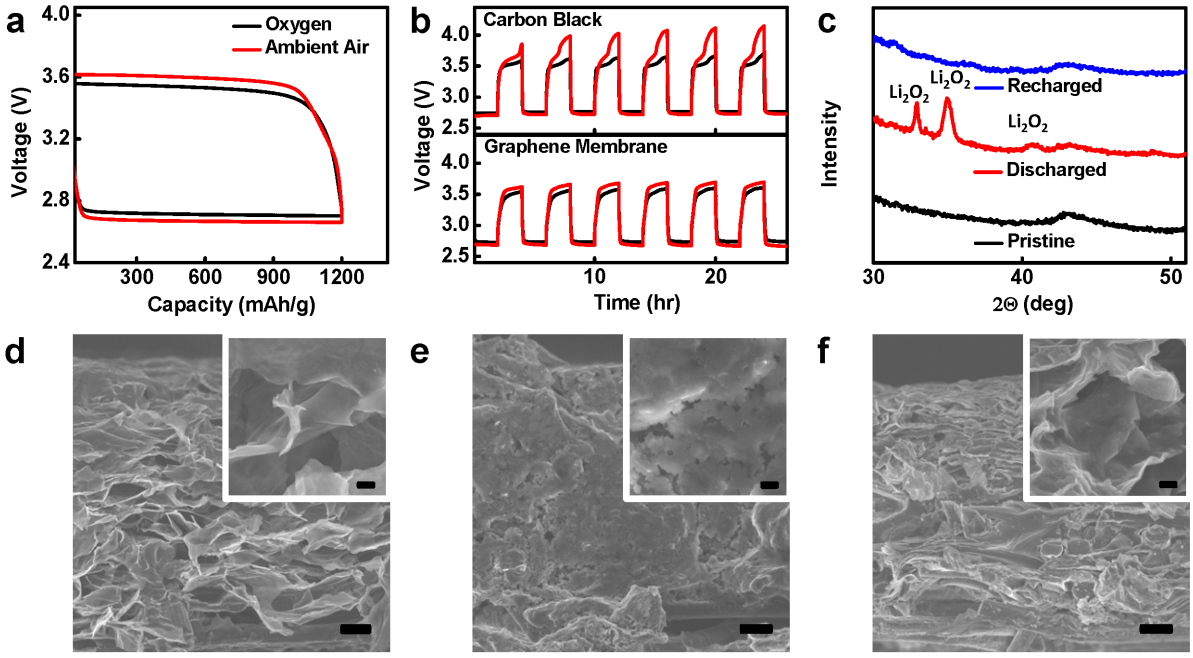

Figure 2.3. Graphene membrane cathode based Li-air cell performance in ambient air and cathode analysis. (a) Galvanostatic discharge/charge curve for graphene membrane cathode based Li-air cell in oxygen and ambient conditions. (b) Galvanostatic cycling of carbon black cathode based Li-air cell (top) and graphene membrane cathode based Li-air cell (bottom) in pure oxygen (black) and ambient air (red). (c) XRD analysis of a pristine graphene cathode, a discharged graphene membrane cathode and a recharged graphene cathode. Cross sectional SEM image of (d) pristine, (e) discharged and (f) recharged graphene cathode. Scale bars are 10 μm and 1 μm (inset).

The severe polarization observed in carbon black cathode under ambient conditions is largely attributed to the moisture in the air, which could react with Li_2O_2 to form non-rechargeable side-products (e.g. LiOH).[56] Additionally, upon deep charge/discharge cycling and accumulation of side-products, the carbon black particles may disintegrate and lose the physical integrity and electrical connection with their surroundings. Excitingly, the 3D graphene membrane cathode shows highly stable charge and discharge characteristics over multiple cycles with little voltage polarization in both pure oxygen (black curve in Figure 2.3b bottom) and ambient conditions (red curve in Figure 2.3b bottom), suggesting that most of the Li_2O_2 is well retained in its original form during these cycles and thus can be converted back to lithium and oxygen when charging without voltage polarization under ambient conditions. This may be attributed to combined effect of highly interconnected 3D conducting network and effective retardation of moisture diffusion by the hydrophobic dense membrane structure.

We have further conducted X-ray diffraction (XRD) studies to analyze the discharge product (Figure 2.3c). The discharged cathode under ambient conditions displays diffraction peaks at 33^o, 35^o, 41^o, which are absent from both the pristine and recharged graphene cathodes. This discharge product can be indexed as Li_2O_2, consistent with previous reports.[11] We have also used SEM studies to evaluate the graphene cathode at pristine, discharged and re-charged state. The pristine graphene membrane electrode shows a relatively clean, densely packed structure and tortuous channels (Figure 2.3d). In the discharged state, a large amount of Li_2O_2 particles are clearly seen covering graphene surface and throughout the graphene membrane (Figure 2.3e), consistent with the XRD studies. It also demonstrates that after discharge, the graphene cathode is able to retain its dense 3D interconnected porous network, therefore ensuring electrical conductivity of the graphene network, and sufficient room for oxygen and electrolyte ion

diffusion during the charging and discharging cycles. Upon recharge, almost all the particles disappeared to result in a highly similar graphene membrane structure (Figure 2.3f) to the original 3D network structures (Figure 2.3d), suggesting a complete recharge of Li_2O_2.

The stable operation of Li-air batteries under ambient conditions has typically been a challenge. Water vapour is generally believed to be the main factor responsible for the poor cycling characteristics of Li-air batteries under ambient conditions.[28-29] To this end, an oxygen selective membrane may be used to allow the diffusion of oxygen while slowing down the ingression of water vapour. A primary battery has been demonstrated with a protective oxygen selective membrane by Maxpower group,[28] however, no rechargeable behavior was reported. The introduction of such oxygen selective membranes can increases the fabrication cost and introduces additional mass to degrade the overall energy density of the resulting system.

For an ideal air cathode electrode working under ambient conditions, the cathode should allow efficient oxygen diffusion while effectively retarding moisture diffusion as much as possible. In general, the molecule transmission through the graphene membrane can be attributed to both the Knudsen diffusion, dictated by membrane geometric parameters (e.g. pore size, density, tortuosity etc.), and the surface diffusion, determined by the molecule-graphene interaction[57] Knudsen diffusion can be tuned by creating a thicker and/or denser graphene membrane. However it is not tuneable for gas molecule selectivity. Surface diffusion may be engineered to create a membrane that may allow selective oxygen diffusion. Specifically, on the hydrophobic graphene surface, the chemisorbed oxygen molecule can migrate from one site to another through surface diffusion mechanism.[57] However, water molecules tend to form clusters or even ice crystalline domains on hydrophobic graphene surfaces with little surface diffusion effect.[58-60] Therefore, the surface diffusion of oxygen molecules on hydrophobic graphene is

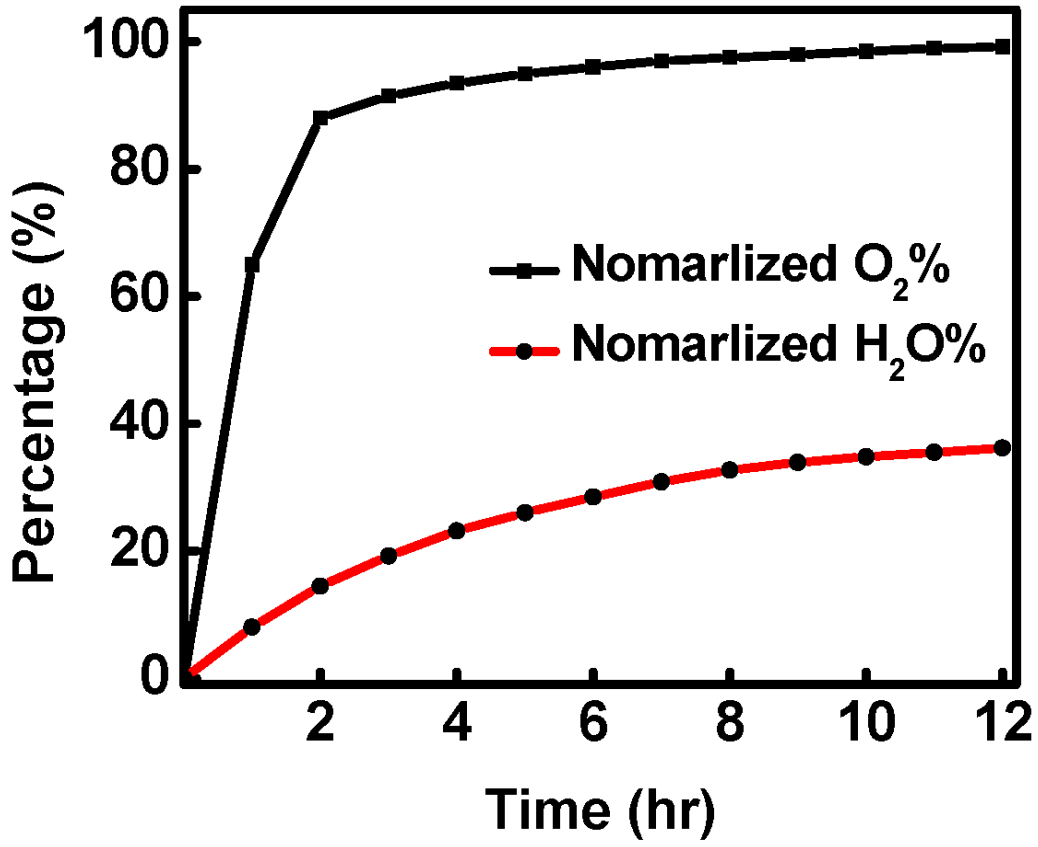

Figure 2.4. Moisture and oxygen diffusion behaviour through the 3D graphene membrane. Normalized oxygen and water concentration within a compartment sealed by a 3D graphene membrane vs. ambient concentration as a function of time, highlighting selective oxygen diffusion (black) vs. water moisture diffusion (red) through the dense graphene membrane.

significantly greater than that of water molecules, resulting in an effective O_2/H_2O selectivity.[61-63]

In practice, a balanced approach has to be taken. An adequate Knudsen diffusion rate and O_2/H_2O selectivity would be both required to create a membrane barrier layer that can sustain sufficient air flow while retaining the O_2/H_2O selectivity for battery operation under ambient

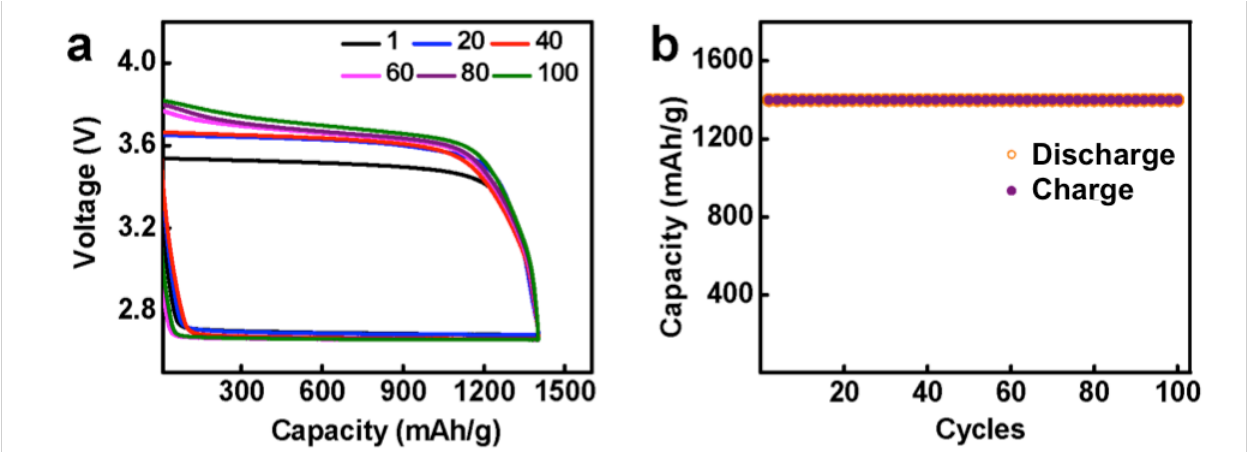

Figure 2.5. Capacity-limited cycling test. (a) Galvanostatic cycling of a Li-air cell with 3D graphene membrane cathode at a capacity of ~1425 mAh g^{-1} (b) Cycling profiles under a capacity of ~1425 mAh g^{-1}in ambient air. Current rate is 2.8 A g^{-1}.

conditions. To validate this hypothesis, we have conducted water and oxygen permeability tests by monitoring the water and oxygen concentration in a chamber sealed with a thin 3D graphene membrane, which clearly shows a much slower diffusion of water molecules than oxygen molecules (Figure 2.4). The moisture concentration increases rather slowly and becomes almost saturated at ~35 % of ambient conditions (~17.8 ^{o}C, ~52.5% relative humidity) after 10 hours. On the other hand, the oxygen shows a much faster diffusion from the beginning and reaches equilibrium with outer atmosphere (~100%) in about 5 hours. Lower moisture penetration can be achieved with a denser/thicker graphene membrane[30] but this could also slow down the oxygen diffusion rate (much lower Knudsen diffusion rate within denser/thicker membrane) and degrade the discharge current. Together, these studies demonstrate that the diffusion rate and O_2/H_2O selectivity can be tuned to meet specific application needs by designing a graphene moisture-resistive membrane with a controlled membrane density and thickness.

To evaluate the cycling stability of our Li-air batteries under ambient conditions, we have cycled the device at different charge/discharge capacities. The Li-air battery is first cycled with a moderate capacity of 1425 mAh g^{-1} (Figure 2.5a). Excitingly, the device displays a highly stable cycling behaviour up to 100 cycles with nearly the same charge/discharge behaviour for each cycle (Figure 2.5b). After 50 cycles, the charge over-potential begins to gradually increase and reaches 3.8 V at 100 cycles. Ren has reported a 3D hierarchical porous graphene electrode and cycled over 100 times at ~1000 mAh g^{-1} which has similar performance with our performance.[40]

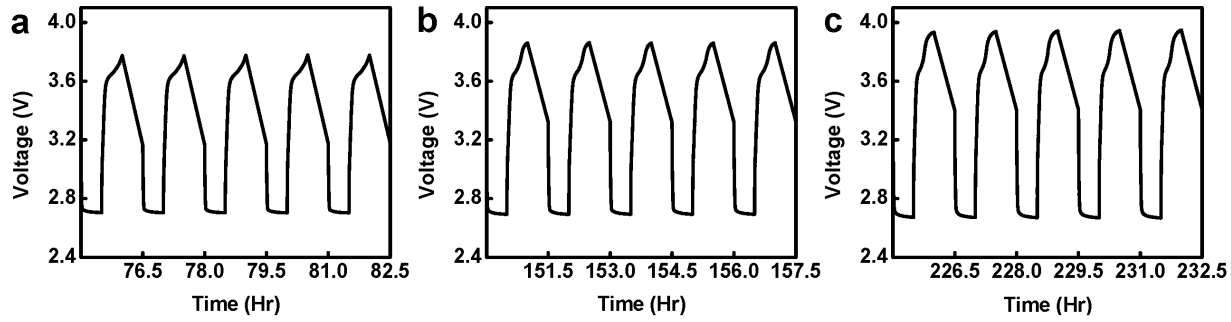

Figure 2.6. Cycling test with 0.5 hour break between cycles. (a) 50^{th} – 55^{th} cycle (b) 100^{th} – 105^{th} cycle (c) 150^{th} – 155^{th} cycle. Current rate is 2.8 A g^{-1}.

However, their battery was operated under the pure O_2, which again demonstrated the superiority of the moisture resistive feature of graphene membrane in this work.

With the repeated cycling at relatively high charge/discharge rate in our test, the cycling induced heat can accumulate, leading to an increased cell temperature that could degrade the cycling performance. In practice, we don't normally expect continuous repeated charge/discharge cycles, but rather with intermittence between charge and discharge cycles. Importantly, with a break between each charge/discharge cycles to allow thermal dissipation, our coin cells can exhibit further improved cycling characteristics with stable cycling endurance up to 200 cycles at the capacity of 1425 mAh g^{-1} (Figure 2.6)

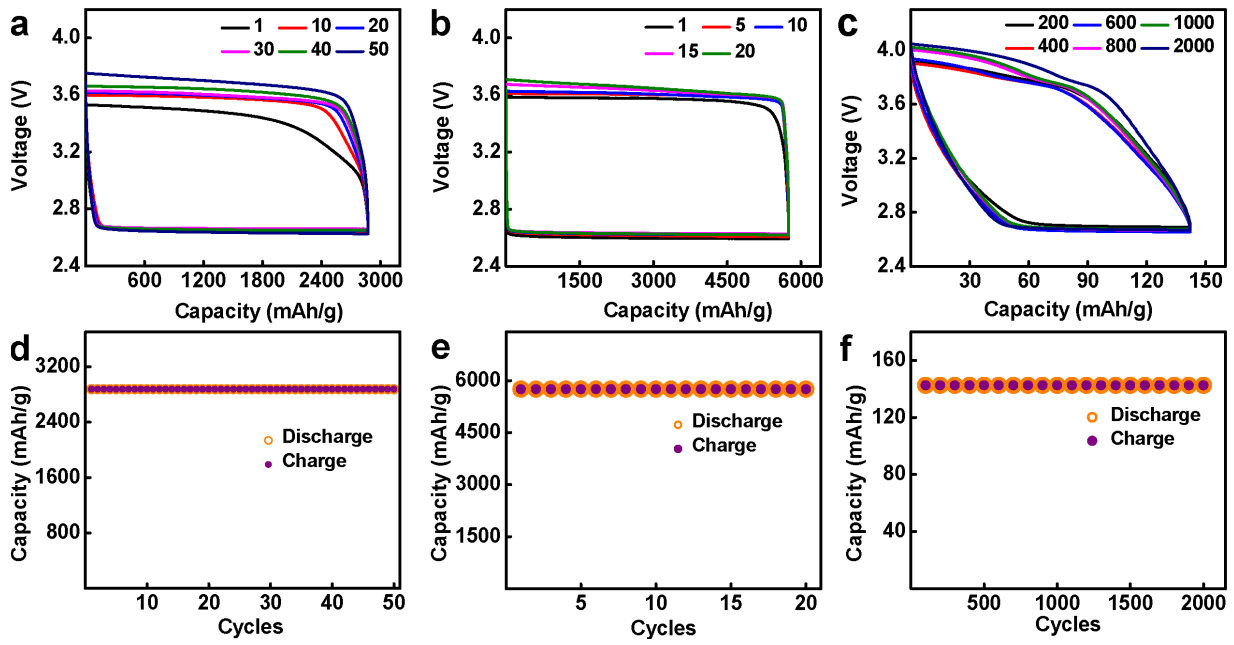

Figure 2.7. Capacity-limited cycling test at variable capacities. Galvanostatic cycling of Li-air cells at a capacity of (a) ~2850 mAh g^{-1}, (b) ~5700 mAh g^{-1}, and (c) ~140 mAh g^{-1} Cycling profiles at a capacity of (d) ~2850 mAh g^{-1}, (e) ~5700 mAh g^{-1} (f) ~140 mAh g^{-1} in ambient air. Current rate is 2.8 A g^{-1}.

To further evaluate the operation stability at a deeper discharge state, we have conducted cycling tests at a capacity of 2850 mAh g^{-1} and 5700 mAh g^{-1} (Figure 2.7a, b). Discharge capacity is readily achieved with little charge polarization for 50 cycles (Figure 2.7d) and 20 cycles (Figure 2.7e) respectively. We have also conducted the cycling test with different graphene membrane thicknesses and have observed highly comparable specific capacity and cycling characteristics. For example, capacity limited galvanostatic cycling on a 40 μm thick

membrane (Figure 2.8) shows excellent discharge capacity (~2850 mAh g^{-1}) and cycling stability over 50 cycles (Figure 2.8b,c).

Although the 3D graphene membrane air cathode has exhibited stable cycling performance up to 100 cycles, the cycle life is still far from a Li-ion battery cathode, which is typically over 1000 cycles. On the other hand, it is important to note that our graphene

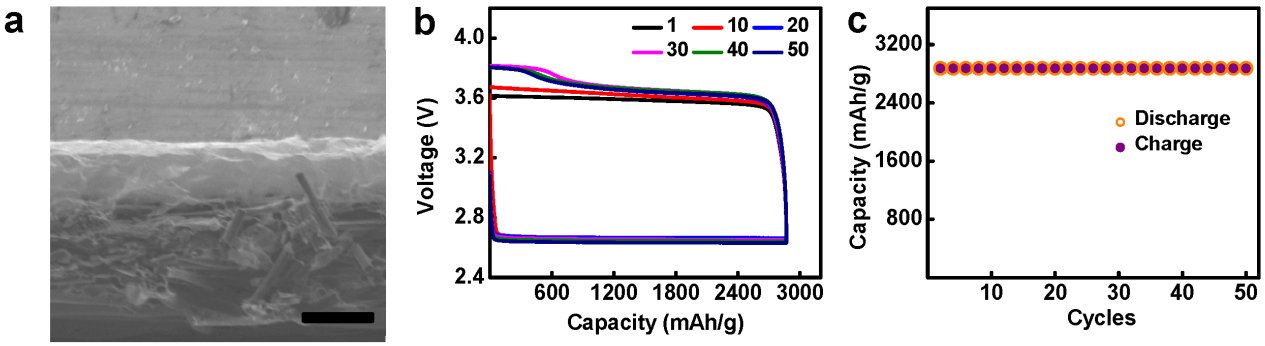

Figure 2.8. Capacity-limited test of a Li-air cell with a 40-µm thick 3D graphene membrane cathode. (a) Cross sectional SEM image of a 40 µm graphene membrane cathode. Scale bar is 50 µm (b) Galvanostatic cycling under a capacity limitation of ~2850 mAh g^{-1}. (c) Cycling profiles under a capacity limitation of ~2850 mAh g^{-1}. Current rate is 2.8 A g^{-1}.

membrane air cathode capacity (1400-5700 mAh g^{-1}) greatly exceeds that of Li-ion batteries (120~150 mAh g^{-1}) by 10-40 times. Therefore, the lifespan cathode capacity (single discharge

capacity × cycle number) of the graphene membrane air-cathode is on par with a typical Li-ion battery cathode. With comparable lifespan capacity but much higher single charge capacity, the Li-air battery with graphene membrane air cathode may offer a unique energy storage solution that can greatly increase the battery life (by >10 times) and reduce the frequency of charge cycles, bridging the gap between rechargeable Li-ion batteries and traditional primary batteries. Moreover, by reducing the degree of discharge (lower capacity per cycle), it is also possible to achieve much longer cycle life while holding a capacity comparable to that of Li ion battery cathode. For example, we have performed a cycling test at a capacity of ~140 mAh $g^{-1}$and achieved stable operation over 2000 cycles, which compares well with typical Li-ion battery cathodes (Figure 2.7c,f).

2.4 Conclusion

In summary, our studies demonstrate that a binder-free high capacity air cathode can be constructed using a hydrophobic dense 3D graphene membrane. The 3D graphene membrane structure has a highly interconnected graphene network for efficient charge transport, a highly porous structure for efficient diffusion of oxygen and electrolyte ions, and a large specific surface area for high capacity storage of the discharge product, Li_2O_2. Lastly, the highly tortuous hydrophobic graphene membrane generates O_2/H_2O selectivity and effectively retards moisture diffusion to ensure excellent charge/discharge cycling performance under ambient conditions. Together, these combined features allow us to create a Li-air battery with excellent cycling performance (>2000 cycles with 140 mAh g^{-1} and >100 cycles with 1425 mAh g^{-1}) and extremely high capacitance (>5700 mAh g^{-1}over 20 cycles). Our results demonstrate that a

scalable, high capacity, long life cycles Li-air battery cathode can be achieved by rationally designing the graphene moisture-resistive membrane cathode.

With exceptional high single charge capacity and comparable lifespan capacity and cycling performance to that of a Li-ion battery cathode, the graphene membrane air cathode opens up exciting new opportunities to bridge the gap between traditional rechargeable Li-ion batteries and primary batteries, greatly increasing the battery life and reducing the necessary recharge frequency to meet future challenges for mobile power supplies in diverse areas.

2.5 References

1. Lopez, N.; Graham, D. J.; McGuire Jr. R.; Alliger, G. E.; Shao-Horn, Y.; Cummins, C. C.; Nocera, D. G. Reversible reduction of oxygen to peroxide facilitated by molecular recognition. *Science* **2012**, 335, 450-453.
2. Crowther, O., Meyer, B.; Morgan, M; Salomon, M. Primary Li-air cell development. *J Power Sources* **2012**, 196, 1498-1502.
3. Zhang, H.; Zhong, X.; Shaw, J. C.; Liu, L. X.; Huang, Y.; Duan, X. F. Very high energy density silicide–air primary batteries. *Energy Environ. Sci.* **2013**, 6, 2621-2625.
4. Li, F. J.; Kitaura, H; Zhou, H. S. The pursuit of rechargeable solid-state Li-air batteries. *Energy Environ. Sci.* **2013**, 6, 2302-2311.
5. Debart, A.; Paterso, A.; Bao J; Bruce, P. G. alpha-MnO_2 nanowires: a catalyst for the O_2 electrode in rechargeable lithium batteries. *Angew. Chem. Int. Ed.* **2008**, 47, 4521-4524.
6. Zhang, S. S; Read, J. Partially fluorinated solvent as a co-solvent for the non-aqueous electrolyte of Li/air battery. *J Power Sources* **2011**, 196, 2867-2870.

7. Lu, Y. C.; Gasteiger, H. A.; Parent, M. C.; Chiloyan, V; Yang, S. H. The influence of catalysts on discharge and charge voltages of rechargeable Li–oxygen batteries. *Electrochem. Solid State Lett.* **2010**, 13, A69-A72.

8. Zhong, X.; Zhang, H.; Liu, Y.; Bai, J. W.; Liao, L.; Huang, Y; Duan, X. F. High-capacity silicon–air battery in alkaline solution. *ChemSusChem* **2012**, 5, 177-180.

9. Jung, H. G.; Hassoun, J.; Park, J. B.; Sun, Y. K; Scrosati, B. An improved high-performance lithium–air battery. *Nat. Chem.* **2012**, 4, 579-585.

10. Freunberger, S. A.; Chen, Y. H.; Drewett, N. E.; Hardwick, L. J.; Bard, F.; Bruce, P. G. The Lithium-oxygen battery with ether-based electrolytes. *Angew. Chem. Int. Ed.* **2011**, 50, 8609-8613.

11. Walker, W.; Giordani, V.; Uddin, J.; Bryantsev, V. S.; Chase G. V.; Addison, D. A rechargeable Li-O_2 battery using a lithium nitrate/N,N-dimethylacetamide electrolyte. *J. Am. Chem. Soc.* **2013**, 135, 2076-2079.

12. McCloskey, B. D.; Scheffler, R.; Speidel, A.; Bethune, D. S.; Shelby, R. M; Luntz, A. C. On the efficacy of electrocatalysis in nonaqueous Li-O_2 batteries. *J. Am. Chem. Soc.* **2011**, 133, 18038-18041.

13. Xiao, J.; Wang, D. H.; Xu, W.; Wang, D. Y.; Williford, R. E.; Liu, J.; Zhang, J. G. Optimization of air electrode for Li/air batteries. *J. Electrochem. Soc.* **2010**, 157, A487-A492.

14. Li, Y. L.; Wang, J. J.; Li, X. F.; Geng, D. S.; Li, R. Y.; Sun, X. L. Superior energy capacity of graphene nanosheets for a nonaqueous lithium-oxygen battery. *Chem. Commun*. **2011**, 47, 9438-9440.

15. Younesi, S. R.; Urbonaite, S.; Björefors, F.; Edström, K. Influence of the cathode porosity on the discharge performance of the lithium–oxygen battery. *J Power Sources* **2011**, 196, 9835-9838.

16. Mitchell, R. R.; Gallant, B. M.; Thompsona, C. V.; Shao-Horn, Y. All-carbon-nanofiber electrodes for high-energy rechargeable Li–O_2 batteries. *Energy Environ. Sci.* **2011**, 4, 2952-2958.

17. Lu, Y. C.; Gasteiger, H. A.; Shao-Horn, Y. Catalytic activity trends of oxygen reduction reaction for nonaqueous Li-air batteries. *J. Am. Chem. Soc.* **2011**, 133, 19048-19051.

18. Zhang, T.; Zhou, H. S. From Li–O_2 to Li–air batteries: carbon nanotubes/ionic liquid gels with a tricontinuous passage of electrons, ions, and oxygen. *Angew. Chem.* **2012**, 124, 11224-11229.

19. Wang, H. L.; Yang, Y.; Liang, Y. Y.; Zheng, G. Y.; Li, Y. G.; Cui, Y.; Dai, H. J. Rechargeable Li–O_2 batteries with a covalently coupled $MnCo_2O_4$ –graphene hybrid as an oxygen cathode catalyst. *Energy Environ. Sci.* **2012**, 5, 7931-7935.

20. Oh, S. H.; Black, R.; Pomerantseva, E.; Lee, J.-H.; Nazar, L. F. Synthesis of a metallic mesoporous pyrochlore as a catalyst for lithium–O_2 batteries. *Nat. Chem.* **2012**, 4, 1004-1010.

21. Suntivich, J.; Gasteiger, H. A.; Yabuuchi, N.; Nakanishi, H.; Goodenough, J. B.; Shao-Horn, Y. Design principles for oxygen-reduction activity on perovskite oxide catalysts for fuel cells and metal–air batteries. *Nat. Chem.* **2011**, 3, 546–550.

22. Xu, J. J.; Wang, Z. L.; Xu, D.; Zhang, L. L.; Zhang, X. B. Tailoring deposition and morphology of discharge products towards high-rate and long-life lithium-oxygen batteries. *Nat. Commun.* **2013**, 4, 2438.

23. Girishkumar, G.; McCloskey, B.; Luntz, A. C.; Swanson, S.; Wilcke, W. Lithium-air battery: promise and challenges. *J. Phys. Chem. Lett.* **2010**, 1, 2193-2203.

24. Chen, L.Y.; Guo, X.W.; Han, J.H.; Liu, P.; Xu, X. D.; Hirata, A.; Chen, M. W. Nanoporous metal/oxide hybrid materials for rechargeable lithium–oxygen batteries. *J. Mater. Chem. A* **2015**, 3, 3620-3626.

25. Peng, Z. Q.; Freunberger, S. A.; Chen, Y. H.; Bruce, P. G. A reversible and higher-rate Li-O_2 battery. *Science* **2012**, 337, 563.

26. Thotiyl, M. M. O.; Freunberger, S. A.; Peng, Z. Q.; Chen, Y. H.; Liu, Z.; Bruce, P. G. A stable cathode for the aprotic Li–O_2 battery. *Nat. Mater.* **2013**, 12, 1050-1056.

27. Li, Y. F.; Huang, Z. P.; Huang, K.; Carnahan, D.; Xing, Y. C. Hybrid Li-air battery cathodes with sparse carbon nanotube arrays directly grown on carbon fiber papers. *Energy Environ. Sci.* **2013**, 6, 3339-3345.

28. Crowther, O.; Salomon, M. Oxygen selective membranes for Li-air (O_2) batteries. *Membranes* **2012**, 2, 216-227.

29. Crowther, O.; Keeny, D.; Moureau, D. M.; Meyer, B.; Salomon, M.; Hendrickson, M. Electrolyte optimization for the primary lithium metal air battery using an oxygen selective membrane. *J Power Sources* **2012**, 202, 347–351.

30. Zhang, J.; Xu, W.; Li, X. H.; Liu, W. Air dehydration membranes for nonaqueous lithium-air batteries. *J. Electrochem. Soc.* **2010**, 157, A940-A946.

31. Huang, S.; Cui, Z.; Zhao, N.; Sun, J.; Guo, X. Influence of Ambient Air on Cell Reactions of Li-air Batteries. *Electrochim. Acta* **2016**, 10, 473-478.

32. Sahapatsombut, U.; Cheng, H.; Scott, K. Modelling of operation of a lithium-air battery with ambient air and oxygen-selective membrane. *J. Power Sources* **2016**, 249, 418-430.

33. Zhang, T.; Zhou, H. S. A reversible long-life lithium–air battery in ambient air. *Nat. Commun.* **2013**, 4, 1817.

34. Lim, H. K.; Lim, H. D.; Park, K. Y.; Seo, D. H.; Gwon, H.; Hong, J. Y.; Goddard, W. A.; Kim, H.; Kang, K. Toward a lithium-air battery: the effect of CO_2 on the chemistry of a lithium-oxygen cell. *J. Am. Chem. Soc.* **2013**, 135, 9733-9742.

35. Novoselov, S.; Geim, A. K.; Morozov, S. V.; Jiang, D.; Zhang, Y.; Dubonos, S. V.; Grigorieva, I. V.; Firsov, A. A. Electric field effect in atomically thin carbon films. *Science* **2004**, 306, 666-669.

36. Bai, J. W.; Zhong, X.; Jiang, S.; Huang, Y.; Duan, X. F. Graphene nanomesh. *Nat. Nanotechnol.* **2010**, 5, 190-194.

37. Xu, Y. X.; Sheng, K. X.; Li, C.; Shi, G. Q. Self-assembled graphene hydrogel via a one-step hydrothermal process. *ACS Nano* **2010**, 4, 4324-4330.

38. Hummers W. S.; Offeman R. E. Preparation of graphitic oxide. *J. Am. Chem. Soc.* **1958**, 80, 1339-1340.

39. He, M.; Zhang, P.; Liu, L.; Liu, B.; Xu, S. Hierarchical porous nitrogen doped three-dimensional graphene as a free-standing cathode for rechargeable lithium-oxygen batteries. *Electrochim. Acta*. **2016**, 191, 90-97.

40. Ren, L.; Hui, K. N.; Hui, K. S.; Liu, Y.; Qi, X.; Zhong, J.; Du, Y.; Yang, J. 3D hierarchical porous graphene aerogel with tunable meso-pores on graphene nanosheets for high- performance energy storage. *Sci. Rep.* **2015**, 5, 14229.

41. Zhang, J.; Li, P.; Wang, Z.; Qiao, J.; Rooney, D.; Sun, W.; Sun, K.; Three-dimensional graphene–Co_3O_4 cathodes for rechargeable Li–O2 batteries. *J. Mater. Chem. A* **2015**, 3, 1504-1510.

42. Zhao, C.; Yu, C.; Liu, S.; Yang, J.; Fan, X.; Huang, H.; Qiu, J. 3D Porous N-Doped Graphene Frameworks Made of Interconnected Nanocages for Ultrahigh-Rate and Long-Life Li–O2Batteries. *Adv. Funct. Mater.* **2015**, 25, 6913-6920.

43. Kim, D.Y.; Kim, M.; Kim, D.W.; Suk, J.; Park, O.O.; Kang, Y. Flexible binder-free graphene paper cathodes for high-performance Li-O_2 batteries. *Carbon* **2015**, 93, 625-635.

44. Guo, X.; Liu, P.; Han, J.; Ito, Y.; Hirata, A.; Fujita, T.; Chen, M. 3D Nanoporous Nitrogen-Doped Graphene with Encapsulated RuO_2 Nanoparticles for Li–O_2 Batteries. *Adv. Mater.* **2015**, 27, 6137-6143.

45. Zhou, W.; Zhang, H.; Nie, H.; Ma, Y.; Zhang, Y.; Zhang, H. Hierarchical Micron-Sized Mesoporous/Macroporous Graphene with Well-Tuned Surface Oxygen Chemistry for High Capacity and Cycling Stability Li–O_2 Battery. *ACS Appl. Mater. Interfaces* **2015**, 7, 3389-3397.

46. Kim, D. Y.; Kim, M.; Kim, D.W.; Suk, J.; Jung Jin Park, Park, O,O.; Kang, Y. Graphene paper with controlled pore structure for high-performance cathodes in Li–O_2 batteries. *Carbon* **2016**, 100, 265-272.

47. Storm, M.M.; Overgaard, M.; Younesi, R.; Reeler, N. E. A.; Vosch, T.; Nielsen, U. G.; Edström, K.; Norby, P. Reduced graphene oxide for Li–air batteries: The effect of oxidation time and reduction conditions for graphene oxide. *Carbon* **2015**, 85, 233-244.

48. Yoo E.; Nakamura, J.; Zhou H. S. N-Doped graphene nanosheets for Li-air fuel cells under acidic conditions. *Energy Environ. Sci.* **2012**, 5, 6928-6932.

49. Xiao, J.; Mei, D. H.; Li, X. L.; Xu, W.; Wang, D. Y.; Graff, G. L.; Bennett, W. D.; Nie, Z. M.; Saraf, L. V.; Aksay, I. A.; Liu, J.; Zhang, J. G. Hierarchically porous graphene as a lithium–air battery electrode. *Nano Lett.* **2011**, 11, 5071-5078.

50. Wang, Z. L.; Xu, D.; Xu, J. J.; Zhang, L. L.; Zhang, X. B. Graphene oxide gel-derived, free-standing, hierarchically porous carbon for high-capacity and high-rate rechargeable Li-O_2 batteries. *Adv. Funct. Mater.* **2012**, 22, 3699-3705.

51. Yoo, E.; Zhou, H. S. Li-air rechargeable battery based on metal-free graphene nanosheet catalysts. *ACS Nano* **2011**, 5, 3020-3026.

52. Lu, Y. C.; Gallant, B. M.; Kwabi, D. G.; Harding, J. R.; Mitchell, R. R.; Whittinghamd, M. S.; Yang, S. H. Lithium-oxygen batteries: bridging mechanistic understanding and battery performance. *Energy Environ. Sci.* **2013**, 6, 750-768.

53. Black, R.; Oh, S. H.; Lee, J. H.; Yim, T.; Adams, B.; Nazar, L. F. Screening for superoxide reactivity in Li-O_2 batteries: effect on Li_2O_2/LiOH crystallization. *J. Am. Chem. Soc.* **2012**, 134, 2902-2905.

54. Younesi, R.; Hahlin, M.; Treskow, M.; Scheers, J.; Johansson, P.; Edstrom, K. Ether based electrolyte, $LiB(CN)_4$ salt and binder degradation in the Li-O_2 battery studied by hard x-ray photoelectron spectroscopy (HAXPES) *J. Phys. Chem. C* **2012**, 116, 18597–18604.

55. Younesi, R.; Hahlin, M.; Bjorefors, F.; Johansson, P.; Edstrom, K. Li-O_2 battery degradation by lithium peroxide (Li_2O_2): a model study. *Chem. Mater.* **2013**, 25, 77–84.

56. Meini, S.; Tsiouvaras, N.; Schwenke, K. U.; Piana, M.; Beyer, H.; Lange, L.; Gasteiger, H. A. Rechargeability of Li-air cathodes pre-filled with discharge products using an

ether-based electrolyte solution: implications for cycle-life of Li-air cells. *Phys. Chem. Chem. Phys.* **2013**, 15, 11478-11493.

57. Burggraaf, A. J. Single gas permeation of thin zeolite (MFI) membranes: theory and analysis of experimental observations. *J. Memb. Sci.* **1999**, 155, 45.

58. Yang D. S.; Zewail, A. H. Ordered water structure at hydrophobic graphite interfaces observed by 4D, ultrafast electron crystallography. *Proc. Natl Acad. Sci. USA* **2009**, 106, 4122-4126.

59. Zheng, Y.; Su, C. L.; Lu, J.; Loh, K. P. Room-temperature ice growth on graphite seeded by nano-graphene oxide. *Angew. Chem. Int. Ed.* **2013**, 52, 8708-8712.

60. Wernet, P.; Nordlund, D.; Bergmann, U.; Cavalleri, M.; Odelius, M.; Ogasawara, H.; Naslund, L. A.; Hirsch, T. K.; Ojamae, L.; Glatzel, P.; Pettersson, L. G. M.; Nilsson, A. The structure of the first coordination shell in liquid water. *Science* **2004**, 304, 995-999.

61. Leenaerts, O.; Partoens, B.; Peeters, F. M. Adsorption of H_2O, NH_3, CO, NO_2, and NO on graphene: A first-principles study. *Phys. Rev. B* **2008**, 77, 125416.

62. Mehmood, F.; Pachter, R.; Lu, W. J.; Boeckl, J. Adsorption and diffusion of oxygen on single-layer graphene with topological defects. *J. Phys. Chem. C* **2013**, 117, 10366-10374.

63. Yan, H. J.; Xu, B.; Shi, S. Q.; Ouyang, C. Y. First-principles study of the oxygen adsorption and dissociation on graphene and nitrogen doped graphene for Li-air batteries. *J. Appl. Phys.* **2012**, 112, 104316.

Chapter 3

3.1 Introduction

Energy storage devices are of increasing importance for applications in mobile electronics, hybrid electric vehicles, and can also play a critical role in renewable energy harvesting, conversion and storage. The lithium-ion battery represents the dominant energy storage technology for mobile power supply today. However, the total capacity of lithium-ion batteries is largely limited by the theoretical capacities of the cathode materials such as $LiCoO_2$ (272 mAh g^{-1}), and $LiFePO_4$ (170 mAh g^{-1}), and cannot satisfy the increasing consumer demand.[1-4] Lithium-sulfur (Li-S) batteries represent the next generation of battery technology, with the sulfur cathode offering a far higher theoretical capacity of 1675 mAh g^{-1}.[5-8] However, there are many challenges associated with Li-S battery technology today, including the intrinsic insulating properties of sulfur and Li_2S, cathode degradation caused by volume expansion/contraction during discharge/recharge process, and the polysulfide shuttling effect.[9-15]

To combat the intrinsic insulating properties of the sulfur, a sulfur cathode is typically prepared by introducing considerable amount of conductive additive and binder to create a composite electrode. Because the conductive additive and binder are typically electrochemically inactive and do not contribute to the energy storage capacity, it is particularly important to minimize the amount of these inactive components and thus maximize the loading ratio of the electrochemically active sulfur in the composite electrodes. Creating a composite electrode with high sulfur content is essential for ensuring high capacity and low production cost for real-world applications.[16-22] However, because of the intrinsically insulating nature and dynamic size change in sulfur, there is considerable challenge in increasing the sulfur-loading ratio while retaining the electrical conductivity and structural integrity of the composite electrode. The

majority of literature to date uses a composite electrode with the sulfur amount typically < 60% of the total weight of the entire cathode (including sulfur, conductive additive and binder).[23] Higher sulfur content up to 80% of the total electrode weight has been reported recently, but the performance of such cathode is yet to be optimized.[19]

Here we aim to explore a three-dimensional graphene framework (3DGF) as a unique conductive scaffold for efficiently loading sulfur particles to create a high performance sulfur cathode.[24-26] The unique structural characteristics and electrical properties of the 3DGF can effectively address many challenges associated with Li-S battery cathodes. First, the highly porous framework structure can allow efficient incorporation of the active sulfur to ensure a high sulfur content up to 80-90%. Second, the conjugated graphene sheets form a continuous network to provide efficient electron transport pathway. The conductivity of the 3DGF can reach up to ~1400 S m^{-1}, enough to counter the insulating properties of sulfur and the discharge products. Third, the hierarchical porous network structure can offer a network of open channels for efficient ion transport. Finally, the individual graphene sheets are conjugated and interlocked together to form a monolithic 3D network that is mechanically strong and can be used as a standalone electrode without extra binders and can withstand repeated expansion and contraction in the charge/discharge cycles.[27-32] Indeed, freestanding 3DGF has recently been explored for Li-S battery electrodes.[19,33,34] The 3DG-sulfur cathodes reported to date were typically prepared via a two-step process by first creating 3DGF followed by infiltrating sulfur, typically with a sulfur content of 60-80% and a highest capacity of only ~500-625 mAh g^{-1} when normalized by the total weight of the cathode material. Here we report a facile one-pot synthesis method to encapsulate sulfur within a freestanding 3DGF to form a 3D graphene-sulfur (3DG-S) composite electrode with a record-high sulfur content of 90%. When used directly as the Li-S battery

cathode without any additives, the 3DGF-S composite electrode displays a capacity of 969 mAh g^{-1} (at 0.1 C), the highest ever value achieved for all sulfur cathodes reported to date when normalized by total electrode mass.

3.2 Experimental

Graphene oxide suspension was synthesized by Hummer's method using natural flake graphite.[35-36] The concentration of the GO suspension obtained was 2.3 g L^{-1}, which was determined by drying the GO suspension at 95°C for 24 hours then weighing.

For a 90% loading three-dimensional graphene sample, 0.1 mL of 1 M $Na_2S_2O_3$ was first mixed with 0.22 mL of 2.3 g L^{-1}GO suspension and 0.58 mL of deionized water. 0.1 mL of 2 M HCl was added drop-wise to the above solution with stirring for 2 hours. 20 μL of 1M ascorbic acid was added to the prior solution, and heated for 2 hours at 95°C to form the hydrogel. After the formation of the 3DG-S composite hydrogel, it was washed several times with water and then freeze-dried. The amounts of the $Na_2S_2O_3$ and HCl were tuned to synthesize 3DG-S70, 80 and 95 using the same method.

Scanning electron microscopy (SEM JEOL 6700) was used to study the morphology of the sulfur cathode. Transmission electron microscopy (TEM T12 Quick CryoEM) was taken to investigate the sulfur infused within the 3D graphene pockets. X-ray Diffraction (XRD) was carried out using a Panalytical X'Pert Pro X-ray Powder Diffractometer with Cu Ka radiation. X-ray photoelectron spectroscopy (Axis Ultra DLD) was used to probe the interactions between sulfur and graphene. TGA was carried out to evaluate the sulfur loading amount using PerkinElmer instruments Pyris Diamond TG/DTA.

The electrochemical properties were carried out by assembly of CR2025 coin cells in an

argon filled glovebox with water and oxygen content kept below 0.1 ppm. The mechanically pressed 3DG-S samples with thickness around 100 μm were directly used as the cathodes and lithium foil was used as the anodes. The electrolyte was a solution of lithium bis(trifluoromethanesulphonyl)imide (1 M) in 1:1 v/v 1,2-dimethoxyethane (DME) and 1,3-dioxolane (DOL) containing $LiNO_3$ (1 wt%). For a typical 3DG-90 cathode, the area was 0.636 cm^2 (the disk with a diameter of 9 mm) and the sulfur mass loading of 3DG-S90 was 4.32 mg cm^{-2}. Galvanostatic charge/discharge cycling was carried out in a potential range of 1.6-2.6 V *vs.* Li/Li^+ with a multichannel battery testing system (LAND CT2001A).

3.3 Results and Discussion

Figure 3.1 schematically highlights the structure of our 3D graphene-sulfur (3DG-S) composite. By uniformly loading sulfur particles into the 3D graphene network, the poor electrical conductivity of sulfur is mitigated by the high electrical conductivity of the graphene network. At the same time, the mechanical stress induced by the volume expansion/contraction during the discharge/charge cycles is also well contained by the flexibility and porosity of the graphene framework. Furthermore, the encapsulation of sulfur particles by the 3D graphene pockets can also inhibit the polysulfide shuttling process to ensure the long duration stability of the electrodes.[20]

The 3D graphene-sulfur (3DG-S) composite electrode was prepared using a facile one-pot synthesis by mixing $Na_2S_2O_3$ and HCl in the presence of graphene oxide (GO) flakes, where the following reaction took place (Equation 1):[37]

$$Na_2S_2O_3 + 2HCl \rightarrow 2NaCl + SO_2 + H_2O + S \quad (1)$$

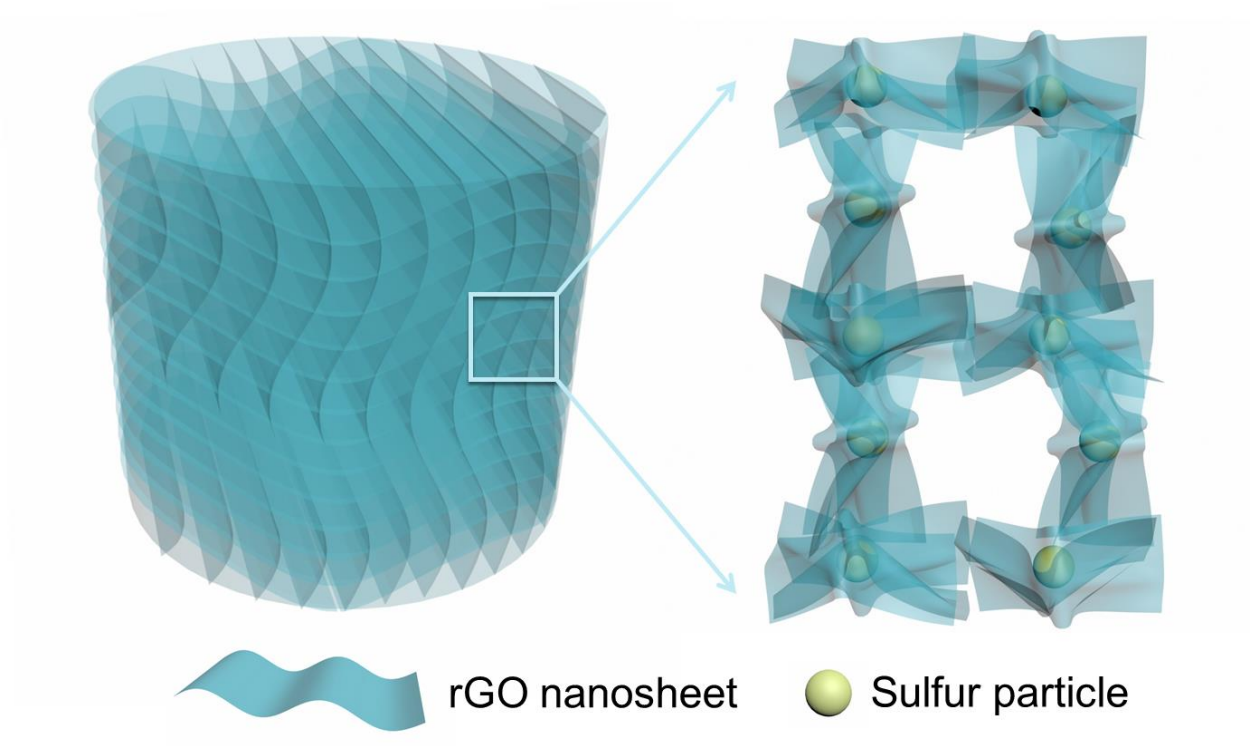

Figure 3.1. Schematic of freestanding 3D graphene-sulfur composite. The left schematic shows a depiction of the three-dimensional structure, and the right schematic illustrates the magnified view of the cross section. The sulfur particles are encapsulated within the 3D graphene pockets.

The formation of 3DG-S composite is induced by introducing the ascorbic acid to drive the reduction of GO and conjugation of the reduced GO into the 3D graphene hydrogel with encapsulated sulfur particles. A photograph of the GO solution shows the typical brownish color (Figure 3.2a, left), while the solution of GO with $Na_2S_2O_3$ and HCl (Figure 3.2a, middle) shows milky cloudy suspension indicating the presence of a large number of sulfur particles.

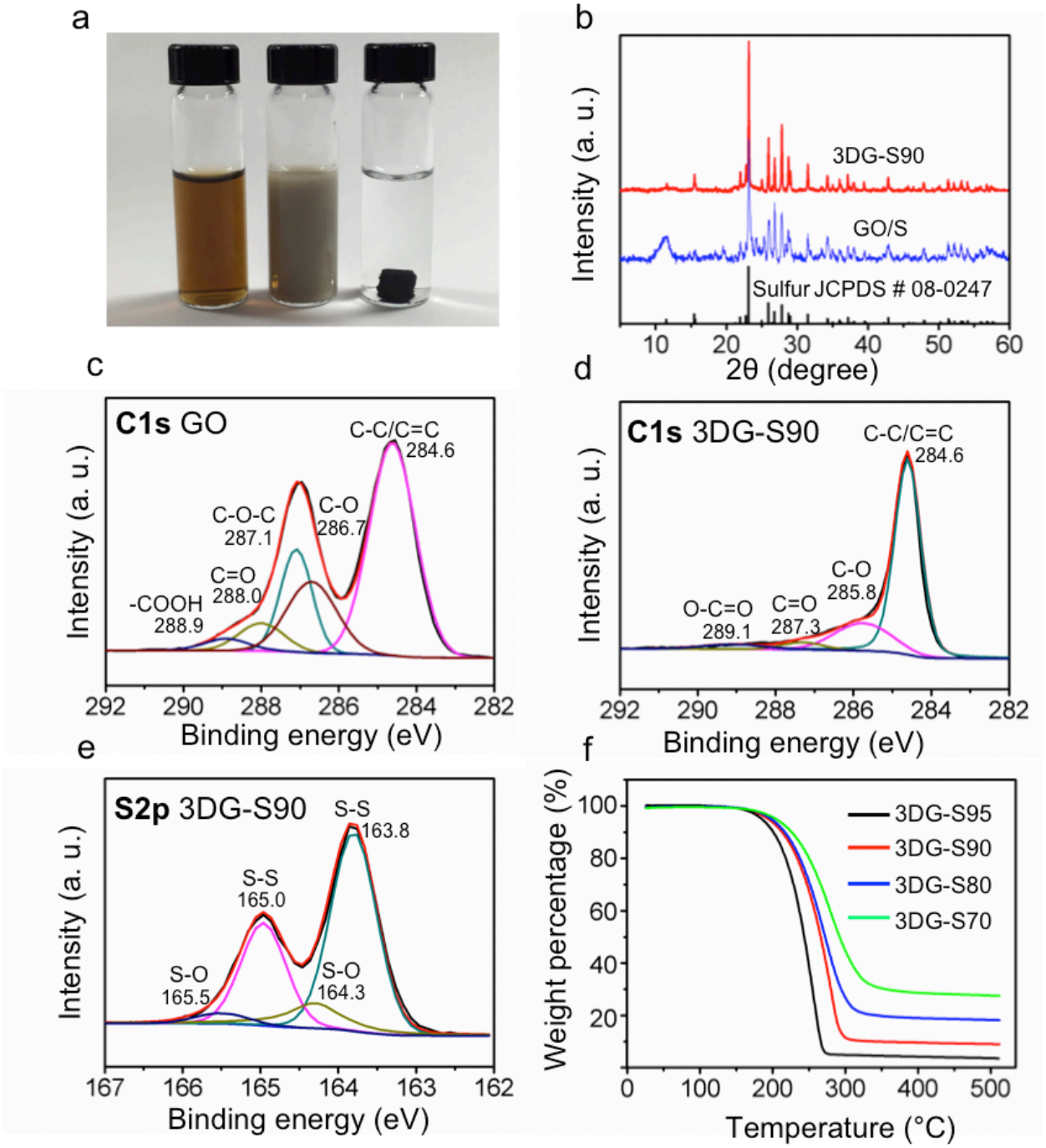

Figure 3.2. (a) Photograph of the solutions of GO, GO with $Na_2S_2O_3$ and HCl, and after reduction of the GO with ascorbic acid, respectively. (b) Comparison of the XRD of pure S_8, GO/S and 3DG-S90. (c) C1s XPS spectrum of pure GO. (d) C1s XPS spectrum of 3DG-S90. (e) S2p XPS spectrum of 3DG-S90. (f) TGA of different 3DG-S samples.

Importantly, with the introduction of the ascorbic acid, a mechanically strong freestanding 3DG-S composite hydrogel can be readily obtained. The photograph of the resulting 3DG-S composite hydrogel in the reaction solution (Figure 3.2a, right) shows a freestanding structure and clear supernatant solution indicating that most of the GO and sulfur particles are conjugated together to form the composite hydrogel with essentially negligible GO or sulfur left in solution. The 3DG-S composite hydrogel was then freeze-dried for subsequent studies. In this way, 3DG-S composites with 70%, 80%, 90% and 95% sulfur.

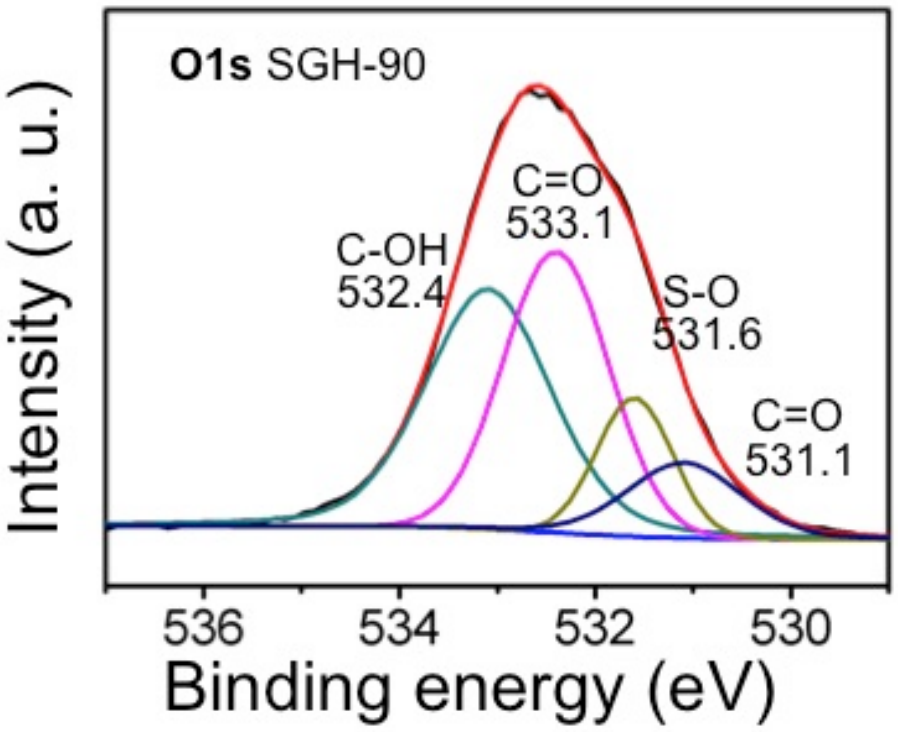

Figure 3.3. O1s XPS spectra of 3DG-S90 demonstrating the S-O peak at 531.6 eV.

We have used X-ray diffraction (XRD) to characterize the 3DG-S90 sample both before and after the reduction process and formation of 3DG-S composite (Figure 3.2b). The initial broad GO peak at 11.6° diminishes after the reduction with ascorbic acid, and the rGO peaks appears at around 22.2°, signifying that the reduction of GO was successful. The XRD spectra shows well-defined diffraction peaks for orthorhombic phase sulfur (JCPDS Card No. 08-0247) in both the samples before and after reduction. To further explore the interactions between the graphene hydrogel and sulfur, X-ray photoelectron spectroscopy (XPS) was conducted (Figure 3.2c-e). Figure 3.2c displays Gaussian fits to the C 1s spectrum of the graphene oxide before the addition of sulfur. The peaks at 284.6, 286.7, 287.1, 288.0, and 288.9 correspond to C-C/C=C, C-O, C-O-C, C=O, and -COOH respectively.[29,33,38] After the reduction of GO and the addition of sulfur, there is a sharp reduction in the peaks representing C=O, O-C=O, and C-O at 289.1, 287.3, and 285.8 respectively, while maintaining a strong C-C/C=C peak at 284.6 as shown in Figure 3.2d. Additionally, the O1s XPS spectrum shows an S-O peak at 531.6 eV (Figure 3.3).[39-41] Sulfur 2p spectrum (Figure 3.2e) is depicted by a doublet with an energy separation of 1.2 eV and an areal ratio of 2:1. The S $2p_{3/2}$ peaks (163.8 and 165.0 eV) are associated with the S-S bonds, and S $2p_{1/2}$ peaks (164.3 and 165.5), associated with the S-O bond.[42] The interaction between S and the residual oxygen on the rGO could help stabilize cycling performance of the composite electrode. The above analysis agrees well with previous literature,[33,38-42] and confirms the interaction between the graphene hydrogel and sulfur. We have also determined the surface area of our 3DG with and without sulfur using Methylene blue absorption test as used in previous studies,[27,29] and found that both the 3DG with or without sulfur loading exhibit a highly comparable surface area of approximately 900 m^2 g^{-1} when normalized by the amount of carbon,

indicating that the inclusion of the sulfur particles does not significant impact on the overall structure the 3D graphene framework.

It is important to control the sulfur content in the 3DG-S composite to ensure optimum cathode performance. To this end, the amount of sulfur particles wrapped within the 3D graphene framework can be readily tuned by controlling the concentration of the sulfur precursor in the GO solution. Thermogravimetric analysis (TGA) was performed to determine the amount of sulfur loaded in the composite structure.[43-44] The TGA studies of the 3DG-S composites show

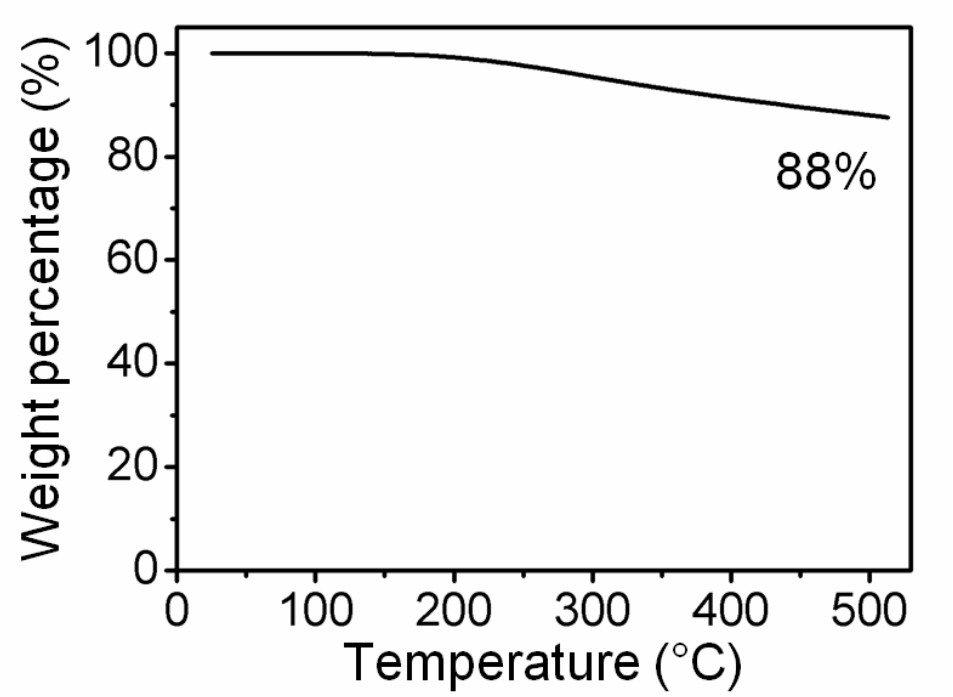

Figure 3.4. TGA of rGO control.

an obvious weight loss when the temperature is increased above 200 ^{o}C (Figure 3.2f), corresponding to sulfur sublimation temperature. To precisely determine the sulfur content, we have also conducted TGA of the pure 3DGF to account for the weight loss contribution from the graphene framework itself (Figure 3.4). After the calibration of weight loss from the pure 3DGF, we can determine the samples with sulfur contents of 70%, 80%, 90%, and 95%.

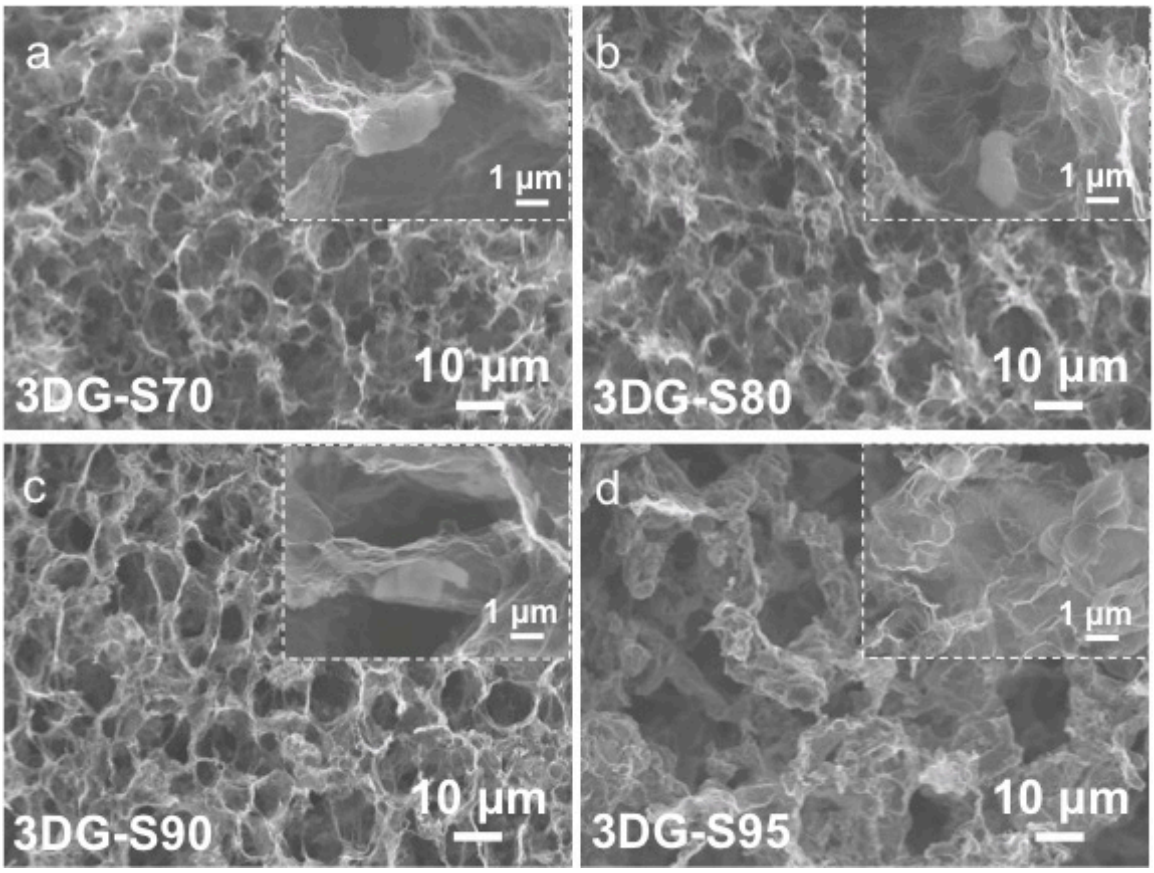

Figure 3.5. Low- and high-magnification (inset) SEM images of (a) 3DG-S70, (b) 80, (c) 90 and (d) 95, respectively

The scanning electron microscopic (SEM) images of the cross-section view of 3DG-S70, 80, 90, and 95 composite show the highly porous graphene framework structures. The 3DG-S70, 80, 90 show similar porous structures with pore sizes typically on the micron scale and comparable sulfur particle size around 1 μm (Figure 3.5a-c). When the sulfur content is increased to 95%, the 3DG-S95 shows rather distinct structural features (Figure 3.5d), with the sulfur particles covering the majority of the graphene sheets and the sample being mechanically very fragile. It should be noted that, for the same amount of graphene, the sulfur mass more than doubles when the sulfur content increases from 90% to 95%.

We have used transmission electron microscopy (TEM) studies to evaluate the encapsulation of sulfur within 3D graphene pockets (Figure 3.6a). Sulfur particles can be seen wrapped around by the graphene. With the strong electron beam irradiation under the TEM, we melted the enwrapped sulfur particles and observed its dynamic flow within the 3D graphene pocket without leaking out onto the copper grid (Figure 3.6b-f, and Supporting video S1), confirming that the sulfur is well encapsulated within the graphene framework with multi-level pockets. Figure 3.6b-d showcases the melted sulfur flowing across graphene wall-1, but then been stopped by graphene wall-2 of the graphene pocket as seen in Figure 3.6e-f. This multiwall feature of the 3D graphene pocket can efficiently inhibit the leakage of the liquid sulfur. The solid-liquid phase transformation of sulfur into soluble polysulfide in the electrolyte during the discharge process is similar to the observed melting process, suggesting that encapsulation of sulfur by 3D graphene pockets may be an effective way to retard the polysulfide shuttling effect.[45]

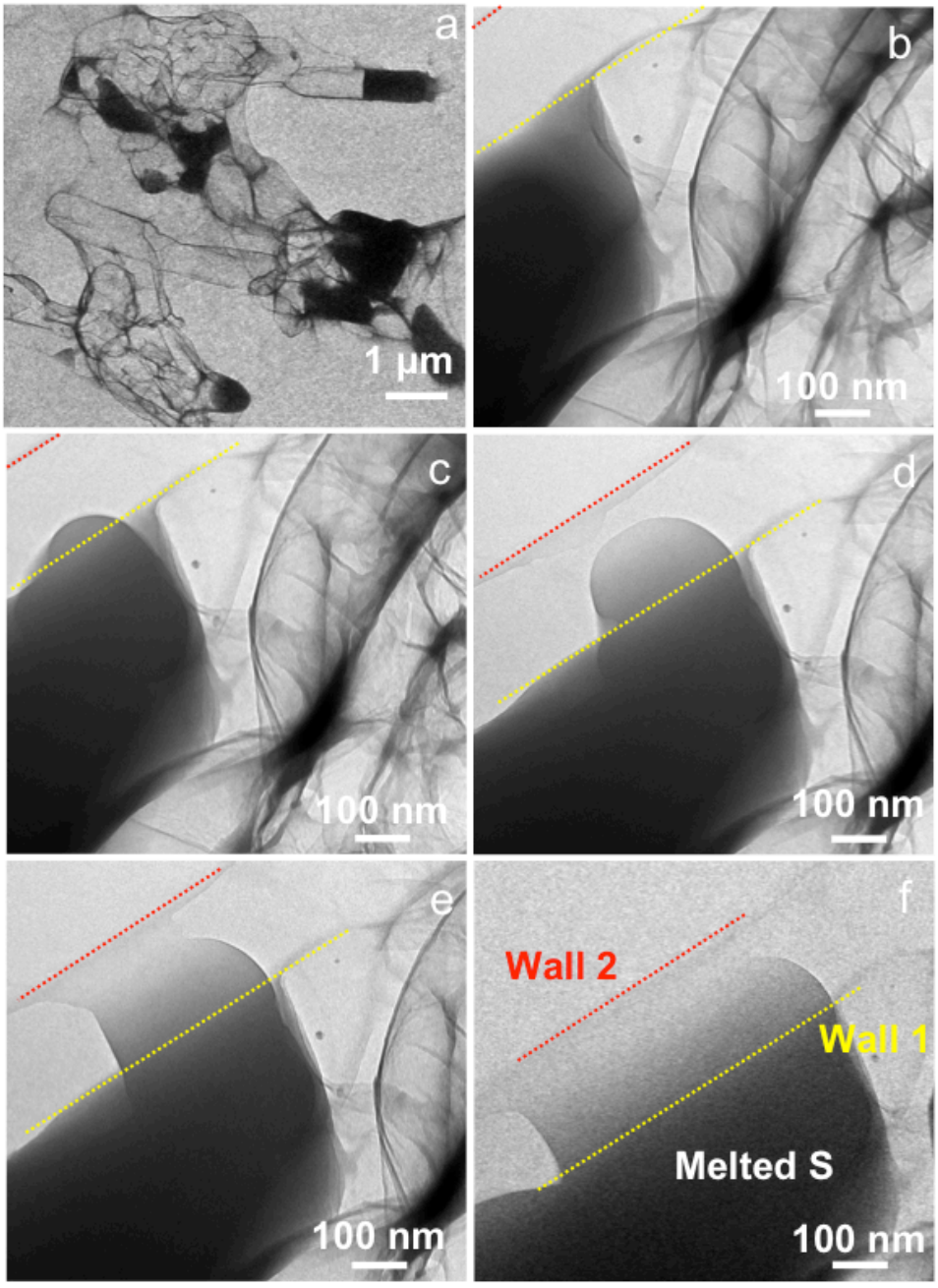

Figure 3.6. (a) Low- magnification TEM image of sulfur particles encapsulated in the 3D graphene pockets. (b-f) Multiple frames of the movement of melted sulfur contained within the graphene pocket. The dotted lines indicate the walls of the graphene pocket.

With the successful preparation of the mechanically strong 3DG-S composites with ultra-high sulfur content, we have further evaluated their electrochemical performance by directly using the freeze-dried 3DG-S composites as the freestanding cathodes without any other additives. Galvanostatic testing was performed in the voltage range of 1.6-2.6 V (*vs.* Li^+/Li). Figure 3.7a shows the discharge/charge curves of 3DG-S90 at 0.1 C. Two plateaus are present, one at 2.32 V and another at 2.08 V, indicative of the formation of long-chain (Li_2S_x, $4 \leq x \leq 8$) and short-chain polysulfides (Li_2S_2 or Li_2S).[46] The discharge/charge curves of the 20th and 50th cycles also clearly showcase the two plateaus, indicating the good electrochemical stability of such cathode. On the first cycle, we achieved an extraordinary capacity of 1070 mAh g^{-1} with 90 wt% sulfur. Figure 3.7b showcases the different 3DG-S samples cycling at 0.1 C where the capacity is normalized only by the sulfur content. The initial capacities for 3DG-S70, 80, 90 and 95 are 1286, 1200, 1077 and 628 mAh g^{-1}, respectively. As expected, when the sulfur loading is lower, the capacity normalized by sulfur tends to be higher, because less sulfur in the graphene framework means relatively more electron and ion transport pathways to make full usage of the sulfur. After 50 cycles, the capacities decrease to 846, 777, 746, mAh g^{-1} for 3DG-S70, 80 and 90, respectively. It is interesting to note that the specific capacity of 3DG-S95 increases gradually to 673 mAh g^{-1} after 50 cycles, which may be attributed to the excessive insulating sulfur in the framework that needs a long activation process to gradually utilize the deep-buried sulfur.[19]

A major issue with Li-S battery research is how to normalize electrochemical performance. In lithium-ion battery research, there is a standard of about 70-80 wt% active material, and 20-30 wt% binder and conductive additive. For Li-S battery research, researchers usually normalize the capacity by only sulfur. However, with a large variation of sulfur content (30-60% for most

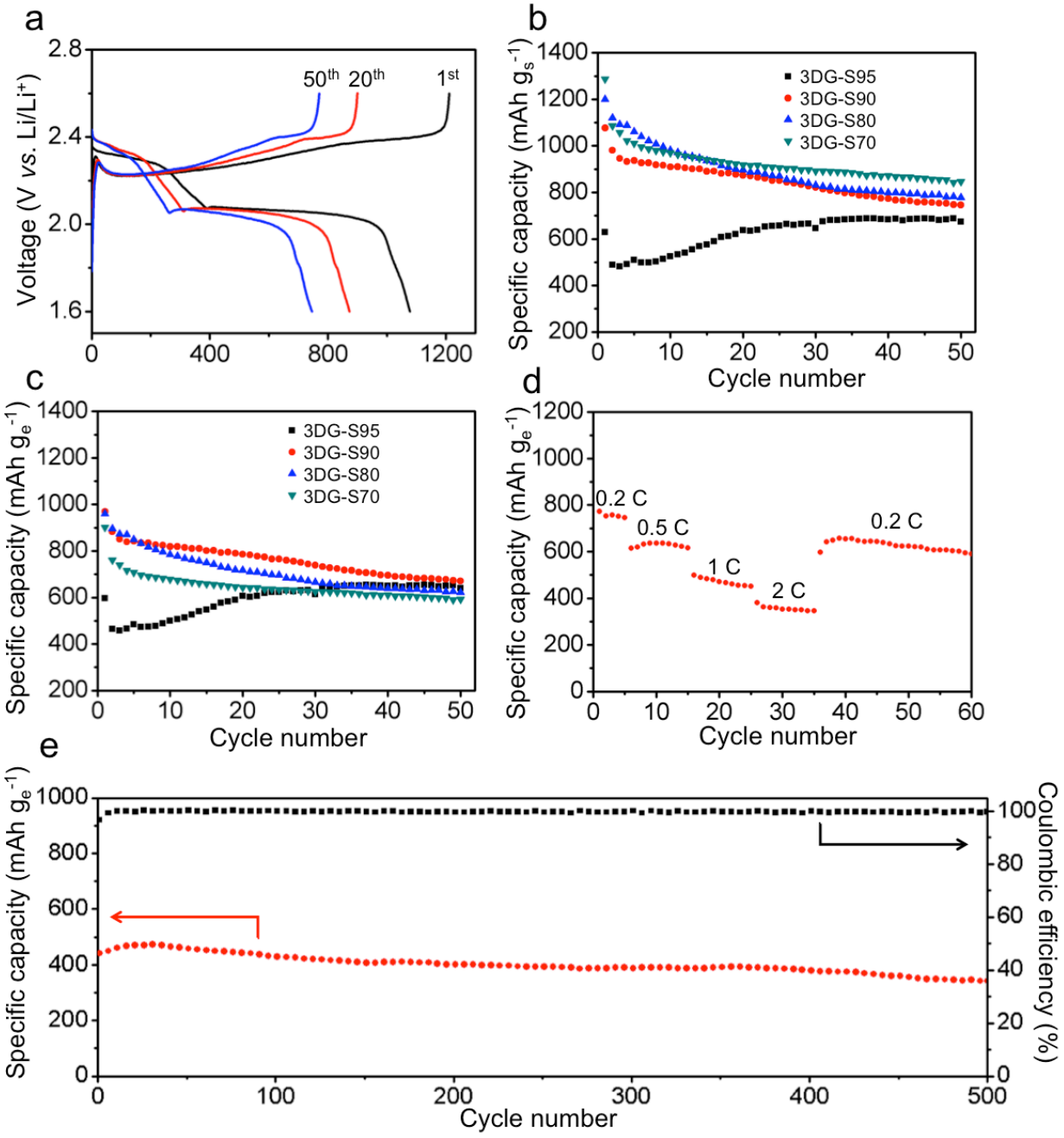

Figure 3.7. (a) Discharge and recharge profile of the 1st, 20th and 50th cycle of 3DG-S90. (b, c) Cycling performance of 3DG-S70, 80, 90, and 95 at 0.1 C with the capacities normalized by (b) only sulfur mass and (c) entire electrode. (d) Rate performance of 3DG-S90 at 0.2 C, 0.5 C, 1 C, and 2 C with the capacities normalized by entire electrode. (e) 3DG-S90 cycling at 1 C for 500 cycles with the capacities normalized by entire electrode.

reports) with different electrode preparation,[18-23] it is difficult to properly compare data obtained in different studies. In general, when normalized only by sulfur, the less sulfur, the higher the capacity is expected (see Figure 3.7b). On the other hand, if we normalize the capacity by the mass of the entire electrode, the 3DG-S90 cathode shows the best performance among all four

Table 3.1. Comparison of the results of this work to reported results. The sulfur content in the composite refers to the percentage of sulfur used before the addition of conductive additive/binder, whereas the sulfur content in the cathode includes the entire electrode mass. Although our capacity is lower compared to literature when normalized only by sulfur, it is considerably higher when normalized by the entire electrode mass.

Ref. No.	Cathode materials	Sulfur content in the composite (%)	Sulfur content in the cathode (%)	Highest capacity normalized by sulfur mass (mAh g^{-1} at 0.1C)	Highest capacity normalized by electrode mass (mAh g^{-1} at 0.1C)
19	Sulfur-graphene sponge	80	80	625	500
18	Aligned carbon nanotube/sulfur composite	90	77	737	564
47	Pomegranate-like carbon cluster-encapsulated sulfur	70	63	1200	756
22	Sulfur/porous graphitic carbon composites	89	62	864	535
8	Nanostructured sulfur/mesoporous carbon materials	70	59	1320	779
44	Monodispersed Sulfur nanoparticles on rGO	70	49	1672	819
This work	**3DG-S90**	**90**	**90**	**1077**	**969**

different samples (Figure 3.7c). Importantly, when normalized by the entire electrode, 3DG-S90 delivers a specific capacity of 969 mAh g^{-1} (at 0.1 C), the highest capacity ever achieved for all sulfur cathodes reported to date (Table 3.1).[7,18,19,22,44,47] Furthermore, when comparing our capacity at different cycles to literature, our capacity is still the highest (Table 3.2). Considering the many methods of preparing a Li-S cathode with high different sulfur content, it is important and essential to display Li-S battery data normalized by entire cathode weight. It is also important to note the C rate is typically normalized by sulfur only. Therefore, if we normalize the power density by total mass of the electrode, the power density of our 3DG-S90 with higher sulfur content would be higher than those of previous reports at the same C rate.

Table 3.2. Comparison of the capacity of 3DG-S90 to reported results at different cycles.

Capacity at cycle for 3DG-S90 (0.1 C)		Capacity at cycle reported (0.1 C)				
Cycle number	Capacity normalized by electrode (mAh g^{-1})	Capacity normalized by entire electrode (mAh g^{-1})				
10	824	444[48]	774[49]	724[50]		
20	790	483[51]				
50	673	591[52]	428[53]	520[54]	585[55]	531[56]

The composite 3DG-S90 is found to have the highest capacity normalized by the entire electrode mass, so it is chosen to investigate the high-rate and cycling performance. Figure 3.7d shows the rate performance of 3DG-S90 normalized by the entire electrode mass from 0.2 C to 2 C. The initial capacities at 0.2, 0.5, 1 and 2 C are 772, 615, 500 and 381 mAh g^{-1}, respectively. It is important to note that due to large intrinsic capacity, the sulfur cathode with 1 C rate can

deliver a power density more than one order of magnitude higher than of conventional lithium-ion battery at 1 C rate. The 3DG-S90 cathode exhibits a good cycling response at various current rates and the capacity is able to recover to 657 mAh g^{-1} at 0.2 C. Figure 3.7e displays the long-life performance of 3DG-S90 cathode at 1 C. The initial specific discharge capacity is 441 mAh g^{-1} normalized by the entire electrode mass. The capacity increases gradually to 473 mAh g^{-1} after 30 cycles due to the activation process. After 500 cycles, the capacity is 341 mAh g^{-1}, corresponding to the capacity retention of 77% and the capacity fading of 0.052% per cycle. After the initial activation process (the first 10 cycles), the Coulombic efficiency stays consistent at 99.5% throughout cycling.

3.4 Conclusion

We have designed and synthesized a freestanding 3D graphene-sulfur composite using a one-pot synthesis method. The combination of the highly conductive interconnected and mechanically strong 3D graphene and the enwrapped sulfur particles has enabled a high performance sulfur-cathode with a record-high capacity of 969 mAh g^{-1} when normalized by the weight of entire cathode at 0.1 C, and stable cycling endurance up to 500 times at 1 C with a capacity fading of 0.052% per cycle. These results demonstrated that the free-standing 3DGF with ultra-high sulfur content can offer a promising pathway to a highly robust Li-S battery.

3.5 References

1. Mizushima, K.; Jones, P.; Wiseman, P.; Goodenough, J. B. Li_xCoO_2 ($0<x\leq1$): a new cathode material for batteries of high energy density. *Mater. Res. Bull.* **1980**, *15*, 783-789.

2. Yamada, A.; Chung, S.-C.; Hinokuma, K. Optimized $LiFePO_4$ for lithium battery cathodes. *J. Electrochem. Soc.* **2001**, *148*, A224-A229.

3. Armand, M.; Tarascon, J.-M. Building better batteries. *Nature* **2008**, *451*, 652-657.

4. Tarascon, J.-M.; Armand, M. Issues and challenges facing rechargeable lithium batteries. *Nature* **2001**, *414*, 359-367.

5. Bruce, P. G.; Freunberger, S. A.; Hardwick, L. J.; Tarascon, J.-M. Li-O_2 and Li-S batteries with high energy storage. *Nat. Mater.* **2012**, *11*, 19-29.

6. Yang, Y.; Zheng, G.; Cui, Y. Nanostructured sulfur cathodes. *Chem. Soc. Rev.* **2013**, *42*, 3018-3032.

7. Ji, X.; Lee, K. T.; Nazar, L. F. A highly ordered nanostructured carbon-sulphur cathode for lithium-sulphur batteries. *Nat. Mater.* **2009**, *8*, 500-506.

8. He, G.; Ji, X.; Nazar, L. High "C" rate Li-S cathodes: sulfur imbibed bimodal porous carbons. *Energy Environ. Sci.* **2011**, *4*, 2878-2883.

9. Lin, T.; Tang, Y.; Wang, Y.; Bi, H.; Liu, Z.; Huang, F.; Xie, X.; Jiang, M. Scotch-tape-like exfoliation of graphite assisted with elemental sulfur and graphene–sulfur composites for high-performance lithium-sulfur batteries. *Energy Environ. Sci.* **2013**, *6*, 1283-1290.

10. Manthiram, A.; Fu, Y.; Chung, S.-H.; Zu, C.; Su, Y.-S. Rechargeable lithium-sulfur batteries. *Chem. Rev.* **2014**, *114*, 11751-11787.

11. Zhang, S. S. Liquid electrolyte lithium/sulfur battery: fundamental chemistry, problems, and solutions. *J. Power Sources* **2013**, *231*, 153-162.

12. Ji, X.; Nazar, L. F. Advances in Li-S batteries. *J. Mater. Chem.* **2010**, *20*, 9821-9826.

13. Zang, J.; An, T.; Dong, Y.; Fang, X.; Zheng, M.; Dong, Q.; Zheng, N. Hollow-in-hollow carbon spheres with hollow foam-like cores for lithium-sulfur batteries. *Nano Res.* **2015,** *8*, 2663-2675.

14. Zhang, K.; Zhao, Q.; Tao, Z.; Chen, J. Composite of sulfur impregnated in porous hollow carbon spheres as the cathode of Li-S batteries with high performance. *Nano Res.* **2013**, *6*, 38-46.

15. Qiu, Y.; Li, W.; Li, G.; Hou, Y.; Zhou, L.; Li, H.; Liu, M.; Ye, F.; Yang, X.; Zhang, Y. Polyaniline-modified cetyltrimethylammonium bromide-graphene oxide-sulfur nanocomposites with enhanced performance for lithium-sulfur batteries. *Nano Res.* **2014**, *7*, 1355-1363.

16. Li, Z.; Jiang, Y.; Yuan, L.; Yi, Z.; Wu, C.;Liu, Y.; Strasser, P.; Huang, Y. A highly ordered meso@microporous carbon-supported sulfur@smaller sulfur core-shell structured cathode for Li-S batteries. *ACS Nano* **2014**, *8*, 9295-9303.

17. Lv, D.; Zheng, J.; Li, Q.; Xie, X.; Ferrara, S.; Nie, Z.; Mehdi, L. B.; Browning, N. D.; Zhang, J. G.; Graff, G. L. High energy density lithium-sulfur batteries: challenges of thick sulfur cathodes. *Adv. Energy Mater.* **2015**, *5*, 1402290.

18. Cheng, X.-B.; Huang, J.-Q.; Zhang, Q.; Peng, H.-J.; Zhao, M.-Q.; Wei, F. Aligned carbon nanotube/sulfur composite cathodes with high sulfur content for lithium-sulfur batteries. *Nano Energy* **2014**, *4*, 65-72.

19. Lu, S.; Chen, Y.; Wu, X.; Wang, Z.; Li, Y. Three-dimensional sulfur/graphene multifunctional hybrid sponges for lithium-sulfur batteries with large areal mass loading. *Sci. Rep.* **2014**, *4*, 4629.

20. Evers, S.; Nazar, L. F. Graphene-enveloped sulfur in a one pot reaction: a cathode with good coulombic efficiency and high practical sulfur content. *Chem. Commun.* **2012**, *48*, 1233-1235.

21. Zheng, J.; Gu, M.; Wagner, M. J.; Hays, K. A.; Li, X.; Zuo, P.; Wang, C.; Zhang, J.-G.; Liu, J.; Xiao, J. Revisit carbon/sulfur composite for Li-S batteries. *J. Electrochem. Soc.* **2013**, *160*, A1624-A1628.

22. Xu, G.-L.; Xu, Y.-F.; Fang, J.-C.; Peng, X.-X.; Fu, F.; Huang, L.; Li, J.-T.; Sun, S.-G. Porous graphitic carbon loading ultra high sulfur as high-performance cathode of rechargeable lithium-sulfur batteries. *ACS Appl. Mat. Interfaces* **2013**, *5*, 10782-10793.

23. Nazar, L. F.; Cuisinier, M.; Pang, Q. Lithium-sulfur batteries. *MRS Bull.* **2014**, *39*, 436-442.

24. Xu, Y.; Sheng, K.; Li, C.; Shi, G. Self-assembled graphene hydrogel via a one-step hydrothermal process. *ACS Nano* **2010**, *4*, 4324-4330.

25. Tang, Z.; Shen, S.; Zhuang, J.; Wang, X. Noble-metal-promoted three-dimensional macroassembly of single-layered graphene oxide. *Angew. Chem., Int. Ed.* **2010**, *49*, 4603-4607.

26. Xu, Y.; Shi, G.; Duan, X. Self-assembled three-dimensional graphene macrostructures: synthesis and applications in supercapacitors. *Acc. Chem. Res.* **2015**, *48*, 1666-1675.

27. Xu, Y.; Chen, C.-Y.; Zhao, Z.; Lin, Z.; Lee, C.; Xu, X.; Wang, C.; Huang, Y.; Shakir, M. I.; Duan, X. Solution processable holey graphene oxide and its derived macrostructures for high-performance supercapacitors. *Nano Lett.* **2015**, *15*, 4605-4610.

28. Xu, Y.; Lin, Z.; Huang, X.; Liu, Y.; Huang, Y.; Duan, X. Flexible solid-state supercapacitors based on three-dimensional graphene hydrogel films. *ACS Nano* **2013**, *7*, 4042-4049.

29. Xu, Y.; Lin, Z.; Huang, X.; Wang, Y.; Huang, Y.; Duan, X. Functionalized graphene hydrogel‐based high‐performance supercapacitors. *Adv. Mater.* **2013**, *25*, 5779-5784.

30. Xu, Y.; Huang, X.; Lin, Z.; Zhong, X.; Huang, Y.; Duan, X. One-step strategy to graphene/$Ni(OH)_2$ composite hydrogels as advanced three-dimensional supercapacitor electrode materials. *Nano Res.* **2013**, *6*, 65-76.

31. Xu, Y.; Lin, Z.; Zhong, X.; Huang, X.; Weiss, N. O.; Huang, Y.; Duan, X. Holey graphene frameworks for highly efficient capacitive energy storage. *Nat. Commun.* **2014**, *5*, 4554.

32. Kim, H.; Lim, H.-D.; Kim, J.; Kang, K. Graphene for advanced Li/S and Li/air batteries. *J. Mater. Chem. A* **2014**, *2*, 33-47.

33. Zhou, G.; Yin, L.-C.; Wang, D.-W.; Li, L.; Pei, S.; Gentle, I. R.; Li, F.; Cheng, H.-M. Fibrous hybrid of graphene and sulfur nanocrystals for high-performance lithium-sulfur batteries. *ACS Nano* **2013**, *7*, 5367-5375.

34. Xi, K.; Kidambi, P. R.; Chen, R.; Gao, C.; Peng, X.; Ducati, C.; Hofmann, S.; Kumar, R. V. Binder free three-dimensional sulphur/few-layer graphene foam cathode with enhanced high-rate capability for rechargeable lithium sulphur batteries. *Nanoscale* **2014**, *6*, 5746-5753.

35. Hummers Jr, W. S.; Offeman, R. E. Preparation of graphitic oxide. *J. Am. Chem. Soc.* **1958**, *80*, 1339-1339.

36. Xu, Y.; Zhao, L.; Bai, H.; Hong, W.; Li, C.; Shi, G. Chemically converted graphene induced molecular flattening of 5, 10, 15, 20-tetrakis (1-methyl-4-pyridinio) porphyrin and its application for optical detection of cadmium (ii) ions. *J. Am. Chem. Soc.* **2009**, *131*, 13490-13497.

37. Gao, X.; Li, J.; Guan, D.; Yuan, C. A scalable graphene sulfur composite synthesis for rechargeable lithium batteries with good capacity and excellent columbic efficiency. *ACS Appl. Mat. Interfaces* **2014**, *6*, 4154-4159.

38. L. Chen, Z. Xu, J. Li, B. Zhou, M. Shan, Y. Li, L. Liu, B. Li, J. Niu. Modifying graphite oxide nanostructures in various media by high energy radiation. *RSC Adv.* **2014**, *4*, 1025.

39. L. Zhang, L. Ji, P.-A. Glans, Y. Zhang, J. Zhu, J. Guo. Electronic sructure and chemical bonding of a graphene oxide-sulfur nanocomposite for use in surperoir performance lithium-sulfur cells. *Phys. Chem. Chem. Phys.* **2012**, *14*, 13670.

40. Y.-H. Yu, Y.-Y. Lin, C.-H. Lin, C.-C. Chan, Y.-C. Huang. High performance polystyrene/graphene-based nanocomposites with excellent anti-corrosion propertires. *Polym. Chem.* **2014**, *5*, 535.

41. C. D. Zangmeister. Preparation and evaluation of graphene oxide reduced at 220°C. *Chem. Mater.* **2010**, *22*, 5625.

42. Z. Wang, Y. Dong, H. Li, Z. Zhao, H. B. Wu, C. Hao, S. Liu, J. Qiu, X. W. D. Lou, *Nat. Commun.* **2014**, *5*, 5002.

43. Sun, L.; Li, M.; Jiang, Y.; Kong, W.; Jiang, K.; Wang, J.; Fan, S. Sulfur nanocrystals confined in carbon nanotube network as a binder-free electrode for high-performance lithium-sulfur batteries. *Nano Lett.* **2014**, *14*, 4044-4049.

44. Chen, H.; Wang, C.; Dong, W.; Lu, W.; Du, Z.; Chen, L. Mono-dispersed sulfur nanoparticles for lithium-sulfur batteries with theoretical performance. *Nano Lett.* **2015**, *15*, 798-802.

45. Rui Xu , J. L., Khalil Amine. Progress in mechanistic understanding and characterization techniques of Li-S batteries. *Adv. Energy Mater.* **2015**, *5*, 1500408.

46. Manthiram, A.; Chung, S. H.; Zu, C. Lithium-sulfur batteries: progress and prospects. *Adv. Mater.* **2015**, *27*, 1980-2006.

47. Li, W.; Liang, Z.; Lu, Z.; Yao, H.; Seh, Z. W.; Yan, K.; Zheng, G.; Cui, Y. A sulfur cathode with pomegranate-like cluster structure. *Adv. Energy Mater.* **2015**, *5*, 1500211.

48. Zhang, K.; Zhao, Q.; Tao, Z.; Chen, J. Composite of sulfur impregnated in porous hollow carbon spheres as the cathode of Li-S batteries with high performance. *Nano Res.* **2013**, *6*, 38-46.

49. Chen, H.; Wang, C.; Dong, W.; Lu, W.; Du, Z.; Chen, L. Mono-dispersed sulfur nanoparticles for lithium-sulfur batteries with theoretical performance. *Nano Lett.* **2015**, *15*, 798-802.

50. Li, W.; Liang, Z.; Lu, Z.; Yao, H.; Seh, Z. W.; Yan, K.; Zheng, G.; Cui, Y. A sulfur cathode with pomegranate - like cluster structure. *Adv. Energy Mater.* **2015**, *5*, 1500211.

51. Ji, X.; Lee, K. T.; Nazar, L. F. A highly ordered nanostructured carbon-sulphur cathode for lithium-sulphur batteries. *Nat. Mater.* **2009**, *8*, 500-506.

52. Li, Z.; Jiang, Y.; Yuan, L.; Yi, Z.; Wu, C.;Liu, Y.; Strasser, P.; Huang, Y. A highly ordered meso@microporous carbon-supported sulfur@smaller sulfur core-shell structured cathode for Li-S batteries. *ACS Nano* **2014**, *8*, 9295-9303.

53. Cheng, X.-B.; Huang, J.-Q.; Zhang, Q.; Peng, H.-J.; Zhao, M.-Q.; Wei, F. Aligned carbon nanotube/sulfur composite cathodes with high sulfur content for lithium-sulfur batteries. *Nano Energy* **2014**, *4*, 65-72.

54. Lu, S.; Chen, Y.; Wu, X.; Wang, Z.; Li, Y. Three-dimensional sulfur/graphene multifunctional hybrid sponges for lithium-sulfur batteries with large areal mass loading. *Sci. Rep.* **2014**, *4*, 4629.

55. Xu, G.-L.; Xu, Y.-F.; Fang, J.-C.; Peng, X.-X.; Fu, F.; Huang, L.; Li, J.-T.; Sun, S.-G. Porous graphitic carbon loading ultra high sulfur as high-performance cathode of rechargeable lithium-sulfur batteries. *ACS Appl. Mat. Interfaces* **2013**, *5*, 10782-10793.

56. Park, M.-S.; Yu, J.-S.; Kim, K. J.; Jeong, G.; Kim, J.-H.; Jo, Y.-N.; Hwang, U.; Kang, S.; Woo, T.; Kim, Y.-J. One-step synthesis of a sulfur-impregnated graphene cathode for lithium-sulfur batteries. *Phys. Chem. Chem. Phys.* **2012**, *14*, 6796-6804.

Chapter 4 Catalysis of cathodic reactions

4.1 Introduction

4.1.1 Catalysis of lithium-air batteries

Lithium-air batteries are able to deliver a significantly higher energy density than that of lithium-ion Batteries. The general structure of a lithium-air batter is (anode$^{\text{Li Metal}}$| electrolyte|cathode$^{\text{Oxygen}}$). The major capacity increase can be derived from the fact that the active cathode material is oxygen gas. The theoretical energy density of lithium is 11,680 Wh/Kg, giving a theoretical specific capacity of 3842 mAh g^{-1}. Unlike a lithium-ion battery, no intercalation reaction occurs in a lithium-air battery. Instead two concerted reactions occur creating a product. During discharge, oxygen is reduced in the cathode and reacts with lithium ions produced from the anode to produce Li_2O_2. During recharge, the oxygen evolution reaction occurs and Li_2O_2 breaks down producing O_2 and Li+.[1]

Although there is an increased capacity in lithium-air batteries, the development of the battery faces numerous problems, such as low round-trip efficiency, short cyclability, the consumption of electrolyte, and a lower capacity than that of theoretical value. This makes using a catalyst pivotal in the roll of a functioning Li-Air battery. The catalyst is able to provide many different roles within the cell. It is potentially able to lower the over-potential of for both discharge and charge. As the oxygen that's needed to be reduced enters the cell, it will adsorb onto the catalyst surface, allowing for better reactivity to create the discharge product, Li_2O_2. A catalysts is also able to further stabilize the cell allowing for longer cycling performance. Dawei Su *et al.* have investigated a Pt_xCo_y alloy that demonstrates a capacity of 3100 mAh g-1 with the catalyst compared to only 600 mAh g^{-1} without it.[2] Yi-Chun *et al*. explored the effects of the active functional platinum and gold nanoparticle catalysts for the reaction kinetics of the oxygen

reduction reaction (ORR) and the oxygen evolution reaction (OER).[3] The results demonstrated that Pt and Au greatly influence the discharge (2.8 V vs. Li) and charge voltages (3.4 V vs. Li) compared to when there is no catalyst (2.6 V vs. Li for discharge, and 4.4 V vs. Li for charge). Au is the most active for ORR and Pt is the most active for OER.

It is difficult to compare the normalized capacities and cycling behavior of other literature, however, because both catalyst size, and catalyst loading can be significantly different between studies. Further complications arise when we compare the electrolytes of these different systems. For example, carbonate based electrolytes are less stable in ORR than other electrolytes.[4] Also it has been demonstrated that different electrolytes synergize differently with different metals, potentially further increasing the differences between literature.[5]

It has been demonstrated that when adding Ni to particular noble metals such as Pt or Pd,[6] it is able to drastically increase the ORR potential of the catalyst. Here we look into the catalytic effect that Pd_3Ni has in a Li-Air battery, by comparing cells that contain ~15% Pd_3Ni to cells with only Pd and just Carbon Black. We show that by adding Ni to Pd, we are able to increase the cyclability of the battery by 100% compared to using no catalyst at all. Compared to using only Pd, we are able to maintain the same amount of cycles while decreasing the amount of Pd by about 30%.

4.1.2 Catalysis of lithium-sulfur batteries

Energy storage devices are of increasing importance for applications in mobile electronics, hybrid electric vehicles, and can also play a critical role in renewable energy harvesting, conversion and storage. The lithium-ion battery represents the dominant energy storage technology for mobile power supply today. However, the total capacity of lithium-ion

batteries is largely limited by the theoretical capacities of the cathode materials such as $LiCoO_2$ (272 mAh g^{-1}), and $LiFePO_4$ (170 mAh g^{-1}), and cannot satisfy increasing consumer demand.[7-10] Lithium-sulfur (Li-S) batteries represent the next generation of battery technology, with the sulfur cathode offering a far higher theoretical capacity of 1675 mAh g^{-1}.[11-14] Furthermore, lithium-sulfur batteries have the ability to exceed both the power and energy density of today's energy storage devices. However, there are many challenges associated with Li-S battery technology today, including the intrinsic insulating properties of sulfur and Li_2S, cathode degradation caused by volume expansion/contraction during discharge/recharge process, and the polysulfide shuttling effect.[15-21]

The intrinsic insulating properties of lithium-sulfur batteries are due to the high resistivity of both the starting active material, elemental sulfur, and the final discharge product Li_2S. Due to this high resistivity, a highly conductive supporting scaffold material must be used for cathode. The most commonly used are activated carbons, or graphene.[12-14] However, even when using these conductive materials in conjunction with sulfur it is difficult to achieve high rate capability due to both poor reaction kinetics and the other two issues.

The second issue with lithium-sulfur batteries is the volume expansion of sulfur on discharge. Unlike lithium-ion batteries that undergo intercalation during charge and discharge with little volume change, lithium-sulfur batteries undergo a series of chemical reaction with rather large volume change. During discharge, sulfur reacts with lithium to form a series of polysulfides, Li_2S_8, Li_2S_6, Li_2S_4, Li_2S_3, and Li_2S_2, before reaching the final discharge product Li_2S. Starting from cyclic octatomic sulfur, S_8, to the final discharge product, Li_2S, there is a volume expansion of 80%.[12] Volume expansion and contraction is detrimental to electrodes due to the fact that it may fragment the electrode material and break the connection with the current

collector. In order to combat the volume expansion of sulfur, three-dimensional graphene or porous activated carbons have been used as flexible and/or porous conductive support/matrix for sulfur.

Although the insulating nature and volume expansion of sulfur present a challenge, the largest issue with lithium-sulfur batteries is the polysulfide shuttling effect. As discussed previously, there are many different intermediates formed during the discharge and recharge reaction within the cell. Of those intermediates, Li_2S_8, Li_2S_6, Li_2S_4, Li_2S_3, are all soluble within the electrolyte of the lithium-sulfur battery. This is harmful to cell performance in two regards. First, during both charge and discharge lithium polysulfides dissolved in the electrolyte are able diffuse across the separator from the cathode to the anode and undergo a parasitic reaction with the anode producing an insulating layer, ruining the cell. Secondly, due to the fact that these polysulfides are able to escape from the cathode, there will be a continuing loss of active material with the continued operation of the battery,[12] leading poor cycling performance.

Many different approaches have been explored to inhibit the polysulfide shuttling effect. One method investigated is physical encapsulation of sulfur while still allowing lithium ions to penetrate. The physical encapsulation layer would trap the polysulfide within, inhibiting their diffusion into the electrolyte. Seh *et al.* encapsulated sulfur within a TiO_2 shell and demonstrated 1000 cycles with a capacity of 800 mAh g^{-1} at 0.5 C.[22] Another method is using the partial charges created by the lithium on the polysulfides to interact electrostatically with other metals that also have a partial charge. For example, Pang et al. used the conductive metal oxide Ti_4O_7 to electrostatically bind to the lithium polysulfides, inhibiting their diffusion and increasing the cell cyclability.[23] Another method utilizes an extra layer of material between the cathode and the separator. Su et al. synthesized a functionalized carbon interlayer and placed it in between the

cathode and separator when making the cell. The functional groups on the carbon interacted with the polysulfides resulting in a cell with high cycle life.[24]

The polysulfide shuttling effect is fundamentally attributed to the soluble reaction intermediates (polysulfides). A fundamental approach to combat the polysulfide shuttling effect is to design/use a sulfur reduction catalyst to create an alternative reaction pathway to completely eliminate the generation of polysulfide intermediates or rapidly transform the polysulfide intermediates into insoluble Li_2S by significantly increase the reaction kinetics. This catalyst approach is attractive for many reasons. First, due to increase of the rate of polysulfide conversion, a significant less amount of active material would be lost during cycling, leading to an extended lifetime of the cell. Second, the cell would be able to perform at a high rate, increasing the power density even at high mass loadings. Most importantly, due to the low amount of catalyst that would be needed, there would be a small amount of weight added to the electrode, enabling higher active material loadings. The lower the mass of the additive, the higher the mass loading of the active material that can be achieved. Indeed, similar concepts have been suggested, but is far under explored to date.[25] In order to fully explore the potential of catalysts, it is important to develop a systematic approach to rapidly prepare and screen a large number catalyst candidates. A major issue with catalysts is discovering which metal, or metal complex demonstrates the best performance at a fast rate. In general, in order to find out whether the metal complex will work as a catalyst, one would have to first make the cathode incorporating the catalyst, make the coin cell, test the coin cell, then finally compare it to other samples. Not only are all these steps time consuming and material intensive, there are many variables introduced that may affect the end performance of the cell. For example, two electrode slurries may have been made slightly different, both containing the same catalysts, but produce

significantly different results. This variance within experiments makes it difficult to determine the exact performance/contribution of the catalyst introduced, and also makes it difficult to compare different potential catalysts.

Here we use single metal atoms to catalyze the SRR for lithium-sulfur batteries. Using single metal atoms we are able to efficiently catalyze SRR while minimizing the weight of the non-active material. To determine the ideal single atom catalyst, we used an efficient screening method, that's fast and reproducible. We will also this same method to identify and optimize the ideal substrate for our catalyst**.**

4.2 Lithium-air battery catalysis

4.2.1 Experimental

Nanosize Pd_3Ni alloy catalysts were prepared through a chemical reduction process. 8 mg of Palladium(II) Acetylacetonate (Alderich, 99%) and 8 mg of Nickel(II) acetylacetonate (Alderich, 99%), and 20 mg Super P Conductive Carbon Black were dispersed and sonicated in 10 mL of Dimethylformamide, then heated to 160°C for 5 hours. After 5 hours, the nanoparticles in the Carbon black were cleaned three times with ethanol, then dried in an oven at 45°C for 2 hours. The particles were then annealed in a furnace under Argon flow for 2 hours at 200°C.

For electrode preparation, Carbon Paper (AvCarb P50) was used as the cathode substrate, and current collector. 20 mg of Catalyst was weighed out and mixed with 4 mg of PVDF. The Carbon Black, Catalyst, PVDF mixture was grinded with a mortar and pestle for 5 minutes. 0.2mL of 1-Methyl-2- pyrrolidone is added to the mortar. The mixture is then pasted onto the carbon paper, and cut to size.

All the cells were assembled in an argon-filled glove box with water and oxygen content kept both less than 0.1ppm. The positive top cover was machine-drilled to create holes to enable gas diffusion. The cell consists of a metallic Li foil anode and the aforementioned Carbon Paper with Catalyst/Carbon Black cathode. A Celgard separator separated the cathode from the anode. 1.5 M solution of Lithium nitrate ($LiNO_3$)/ Dimethyl sulfoxide (DMSO) was used as the electrolyte.

For the test in pure oxygen, the as prepared Li-air cell was kept in a homemade glass chamber, flowing with oxygen when testing. Galvanostatic discharge/charge was performed with Maccor 4340.

Scanning electron microscopy (SEM JEOL 6700) was used to observe the morphology of the air cathode and EDAX. The T12 cryo-electron microscope was used to take images of the nanoparticles after annealing. X-ray Diffraction(XRD) pattern was carried out using Bruker Smart 1000K Single Crystal X-ray Diffractometer.

4.2.2 Results and Discussion

Figure 4.1 displays TEM images of both Pd_3Ni/C and Pd/C after annealing. Both the samples exhibit similar uniformity and morphology. The average size of the particles is approximately 25 nm in diameter. As both the Pd and Pd_3Ni particles are the same size, we are able to compare their effectiveness as a catalyst.

Figure 4.2 shows the X-ray diffraction pattern of Pd_3Ni/C for a solid solution, in which all peaks are in agreement with previously reported face-centered cubic. The blue and red lines represent the location of the standard peaks of Pd and Ni. The sharp peaks at 41.5°, 48°, and 70.1° correspond to the (1 1 1), (2 0 0), and (2 2 0) peaks of the alloy respectively. The shift in

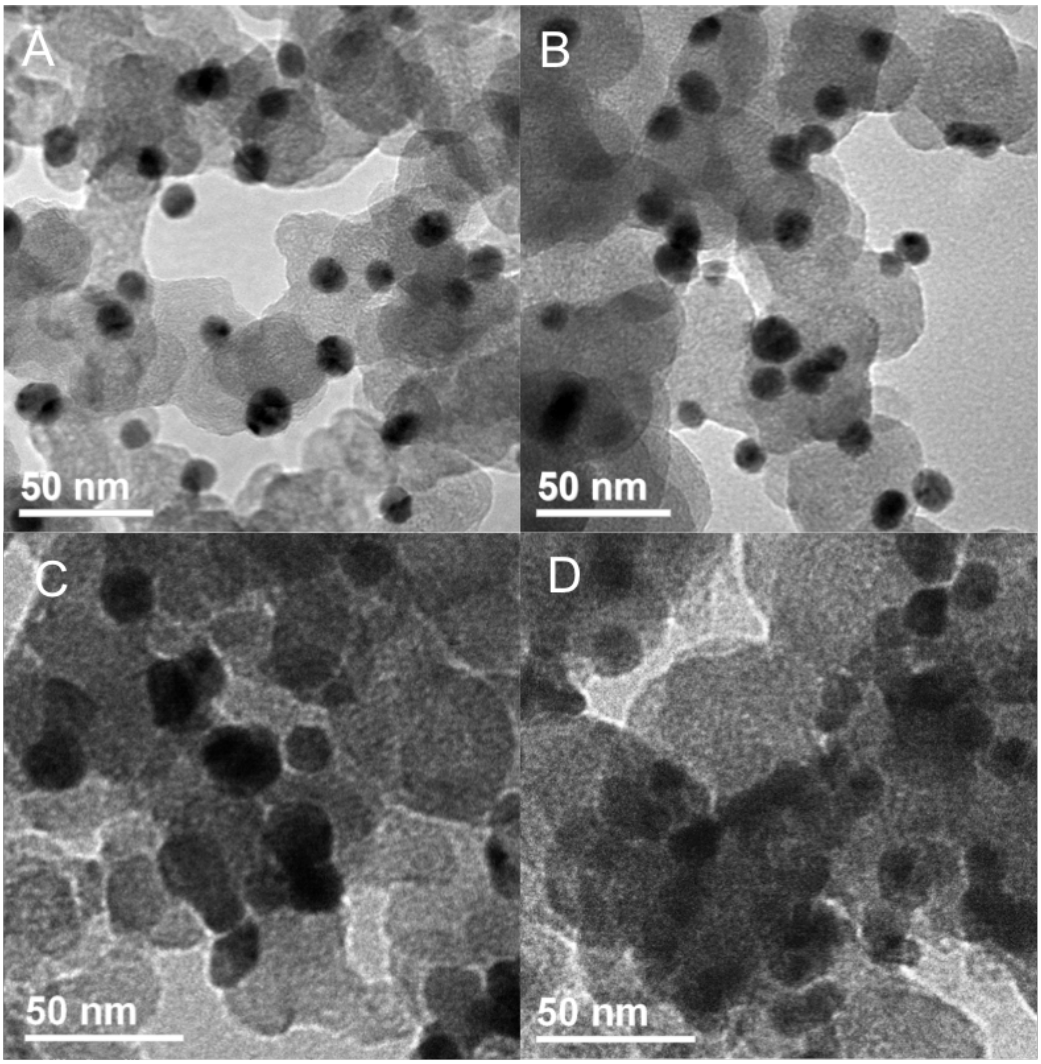

Figure 4.1. TEM images of Pd_3Ni/C and Pd/C, (a) Pd_3Ni/C, (b) Pd_3Ni/C, (c) Pd/C, (d) Pd/C

the peaks compared to the pure Pd signifies the contraction of the lattice due to the incorporation of Ni into the FCC crystal structure of Pd. The ratio of Pd:Ni was determined by the EDX data as seen in Table 4.1. Inductively Coupled Plasma is current been done to determine the exact amount of catalyst synthesized on the activated carbon; however, based on the amount of precursor used, there is approximately 15% catalysts by weight in each cathode.

In order to test the capabilities of the catalyst, galvanostatic testing was conducted. A

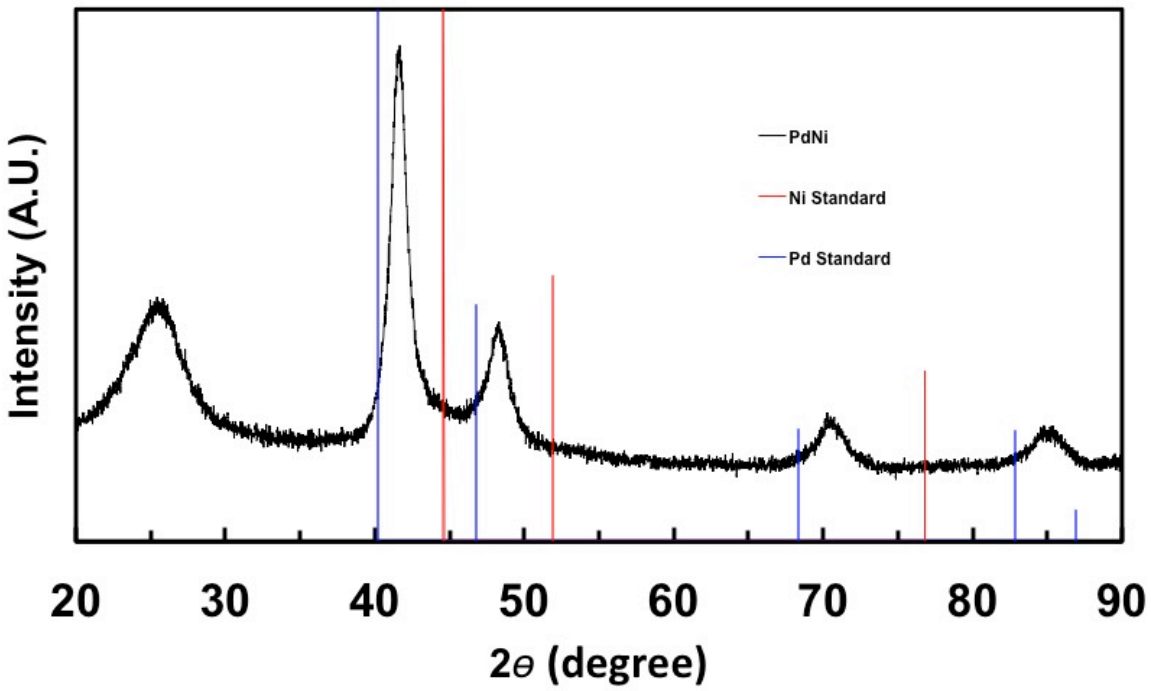

Figure 4.2. X-Ray Diffraction of Pd_3Ni Alloy

Table 4.1. EDX results of Pd_3Ni

Element	Weight %	Atomic %
Pd	64.33	76.57
Ni	35.67	23.43

Super P Carbon Black, Pd/Carbon Black, and Pd_3Ni/Carbon Black were all cycled at 100 mA g^{-1} for 200 mAh g^{-1} cycles in an environment with only O_2. Figure 4.3 displays the cycling data for each of the three cathodes. The carbon black cathode cycles 23 times before becoming unstable. The Pd/C cathode is able to cycles 56 times stably, and the Pd_3Ni/C cathode is able to cycle 53 times stably. Both the Pd/C and Pd_3Ni/C are able to cycle 100% better than the only Carbon

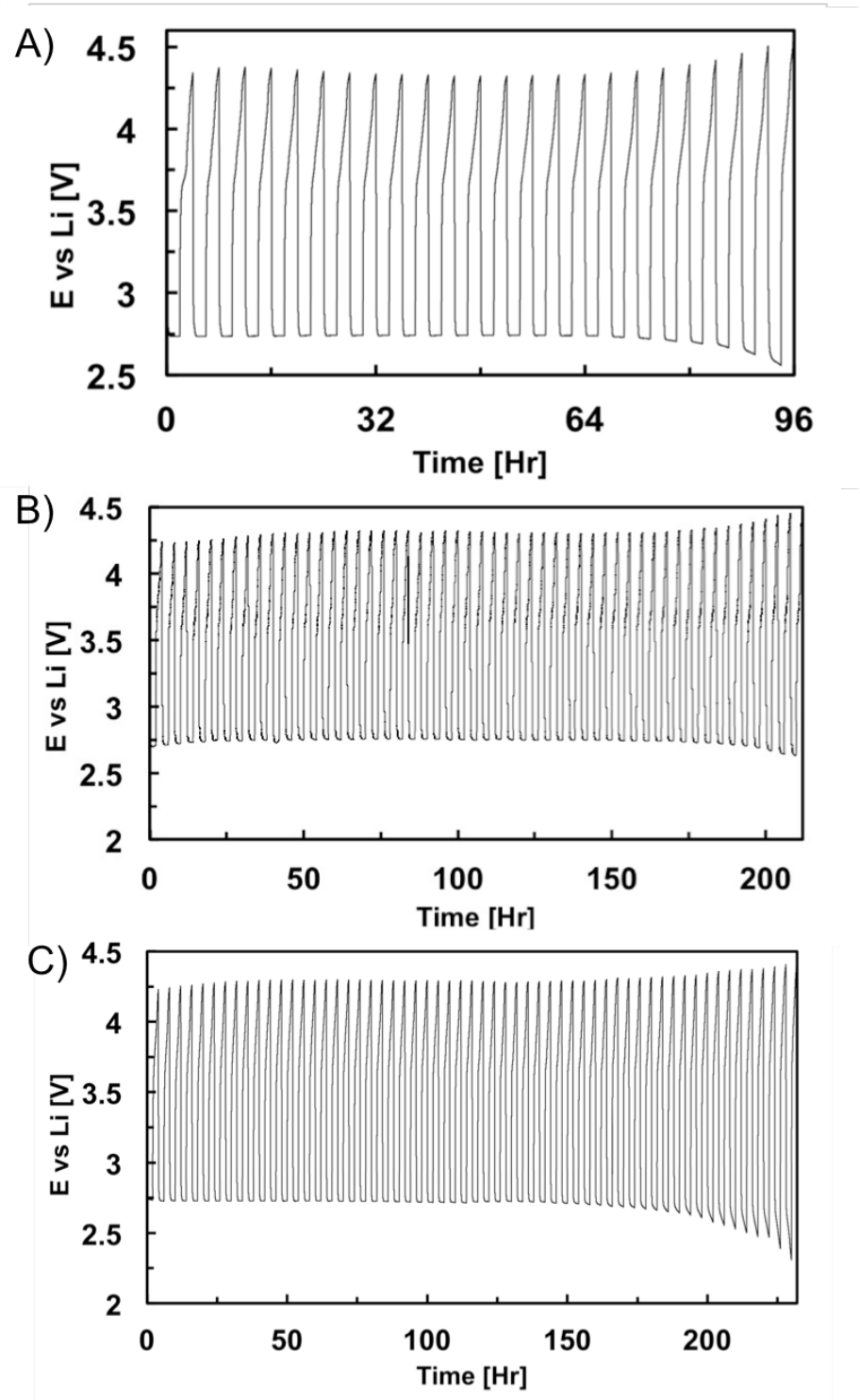

Figure 4.3. Galvanostatic cycling at 100 mA g^{-1} for 200 mAh g^{-1} cycles. (a) Carbon Black Cathode, (b) Pd_3Ni/Carbon Black Cathode, (c) Pd/C Cathode

Black cathode. Although the Pd_3Ni/C and the Pd/C cathodes both cycled approximately the same amount of times, the Pd_3Ni particles contains 30% less Pd per particle. This means that normalized to the amount of Pd per particle, the Pd_3Ni catalyst did perform better than the Pd catalyst. The Pd/C was synthesized using the synthesis method in the experimental section; a comparison between our synthesized Pd/C and commercial Pd/C will also be completed to see the effect difference produced from our synthesis method.

Discharge profiles were also completed to compare the catalyst effect on the discharge capacity at different current densities, as seen in Figure 4.4. When discharged at 100mA g^{-1}, the Pd_3Ni/C cathode has a capacity of 5700 mAh g^{-1}. Carbon Black, on the other hand, when discharged at the same current capacity has a discharge capacity of 4100 mAh g^{-1}. Pd_3Ni/C is able to increase the capacity by approximately 30%. When discharged at a current density of 500mA g^{-1}, the Pd_3Ni/C cathode had a capacity of 2950 mAh g^{-1}, where as using the C only cathode had a capacity of 2050 mAh g^{-1}. This is also approximately a 30% improvement. The increase in capacity that a Pd catalyst achieves is currently been explored.

The reason Pd_3Ni increases both the cyclability and capacity of the Li-Air battery can be attributed to increased reactivity on the nanoparticles surface. Experiments have indicated that only the outer monolayer of the catalyst is involved in reaction 8. Density functional theory calculation demonstrates that the compression of the Pd lattice in PdFe alloys will downshift the d band center, which determines reactivity.[26] Wang et al. predicted ORR performances of Pd based alloys would be enhanced due to the Gibbs free energy of the electron transfer step by alloying.[27] Finally, Xu et al. reported that the enhanced ORR activity on a PdCu catalyst could be attributed to the strained Pd surface with sublayer Cu atoms formed during the replacement process.[28] Therefore, increased reactivity with Pd_3Ni can be attributed to both a surface strain

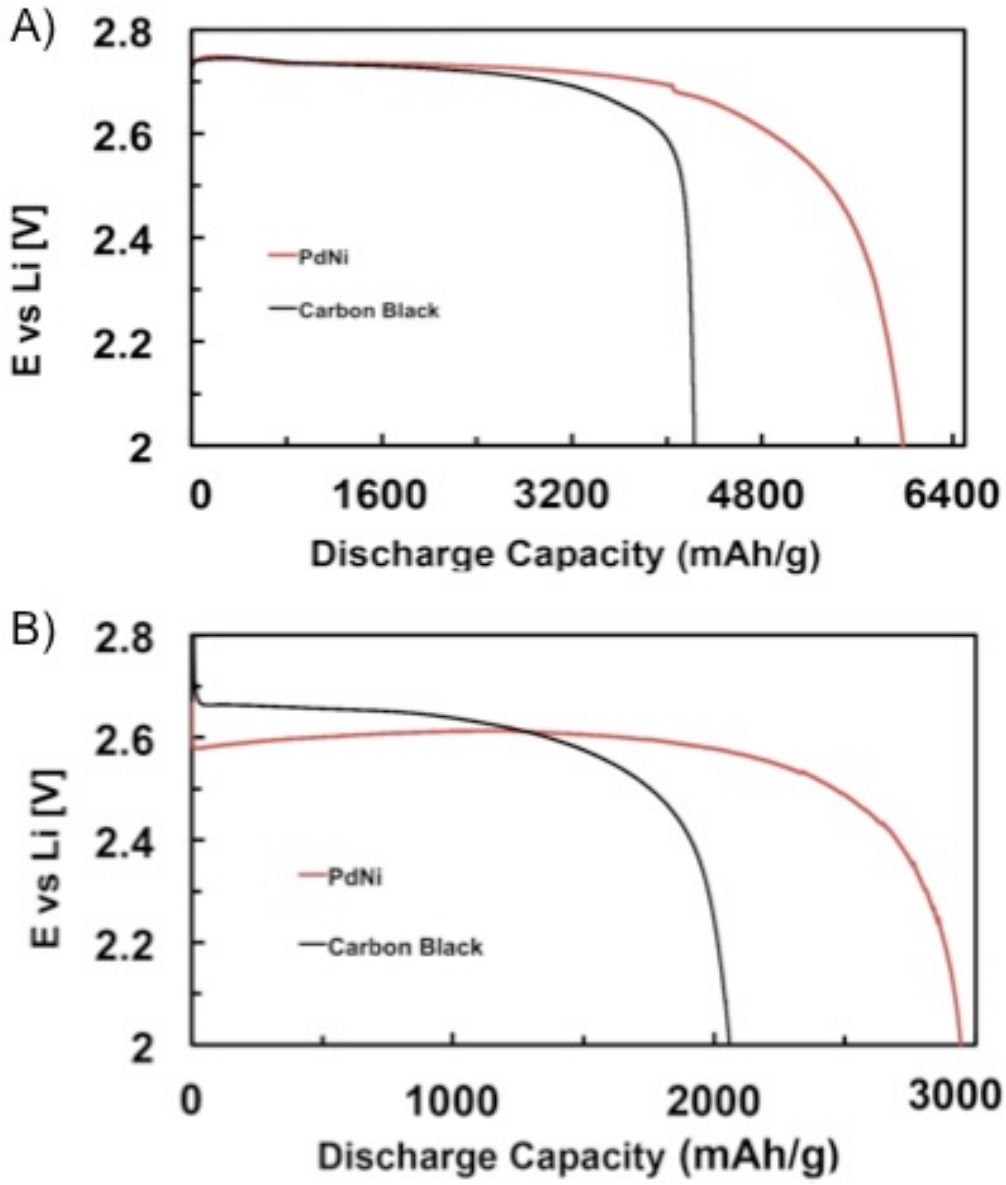

Figure 4.4. Discharge profiles at (a) 100 mA g^{-1} (b) 500 mA g^{-1}

and alloying effect, which could provide distinct sites for the adsorption of small molecules, such as O2, benefitting electrocatalytic reactions.

4.3 Lithium-sulfur Battery Catalysis

4.3.1 Experimental

In order to evaluate catalysts we used a robust, accurate, and faster system that is able to screen our single metal atom catalysts efficiently and effectively for lithium-sulfur batteries. As seen in Figure 4.5, our system is comprised of three distinct aspects: the working electrode, counter/reference electrode, and the electrolyte. However, unlike traditional

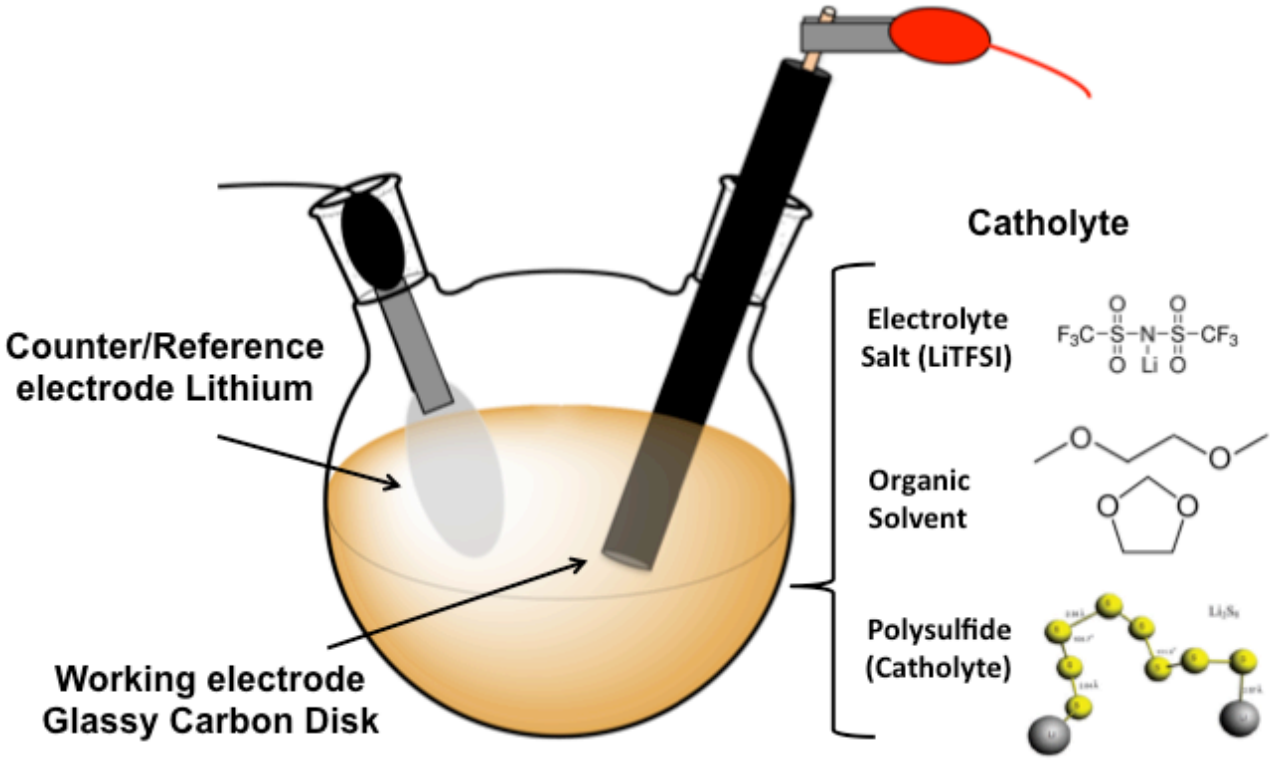

Figure 4.5. Schematic of our proposed potentiostatic set up. The working electrode is a glassy carbon electrode where we are able to deposit the material of choice. Both the counter and reference electrode is thin lithium foil. The electrolyte is our catholyte containing two organic solvents, DOL and DME, an electrolyte salt, LiTFSi, and our synthesized lithium polysulfide.

potentiostatic systems for batteries, our system is an open system (although still in Argon filled glove box with oxygen and water less than 0.1 ppm), in which no battery is assembled. Furthermore, no electrode slurry is necessary; one of the largest factors contributing to variability. The working electrode is a standard glassy carbon electrode. Using the small glassy electrode disk, we are able to load catalyst or a catalyst composite directly onto the electrode. Both the counter and reference electrode in this system will be thin lithium foil.

Graphene oxide suspension was synthesized by Hummer's method using natural flake graphite. The concentration of the GO suspension obtained was 2.3 g L^{-1}, which was determined by drying the GO suspension at 95°C for 24 hours then weighing. The GO was sonicated with a metal precursor of the selected metal for two hours before formation. At most 2% by weight was used in order to look into single atom catalysis. Graphene hydrogels were made hydrothermally at 180°C, then n-doped under ammonia at 900°C for 2 hrs.

Catholyte comprised of 1:1 DOL:DME, with 1M LiTFSi and 1% $LiNO_3$ as well as a 50 mM polysulfide solution, which was created by using a stoichiometric amount of S_8 and Li_2S to mixed under 90°C to synthesize Li_2S_8.

4.3.2 Results and Discussion

Lithium polysulfide was synthesized by adding Li_2S with stoichiometric S_8 to create the polysulfide of choice.[25] One concern with using this electrolyte might be the fact that both the organic electrolyte and the lithium polysulfides themselves are electronically inert, increasing the overpotenital of the overall system. In order to alleviate this problem, a high concentration of electrolyte salt is used as well as placing the working and counter/reference electrodes in close proximity to one another. Since each catalyst will be compared to each other in the exact same

conditions, the slight increase in resistance caused by the electrolyte will be a non-issue. Furthermore, as seen in our study in Figure 4.6, we tuned the concentration of the lithium polysulfides in order to optimize the electrolyte and maintain the distinct redox peak seen in lithium-sulfur batteries.

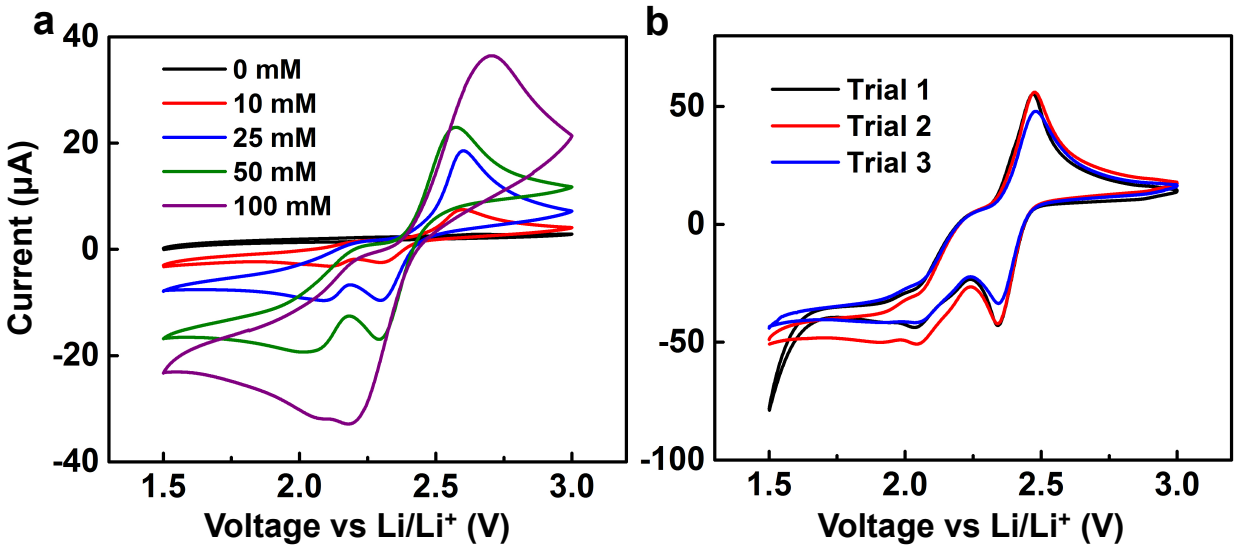

Figure 4.6. (a) Cyclic Voltammetry of bare glassy carbon electrode with different concentrations of lithium polysulfide. As there are no discrete peaks when using a 100 mM solution, a 50 mM or below will be used. (b) Cyclic Voltammetry of three different electrodes with the same amount of activated carbon. Our results demonstrated a standard deviation of less than 3%

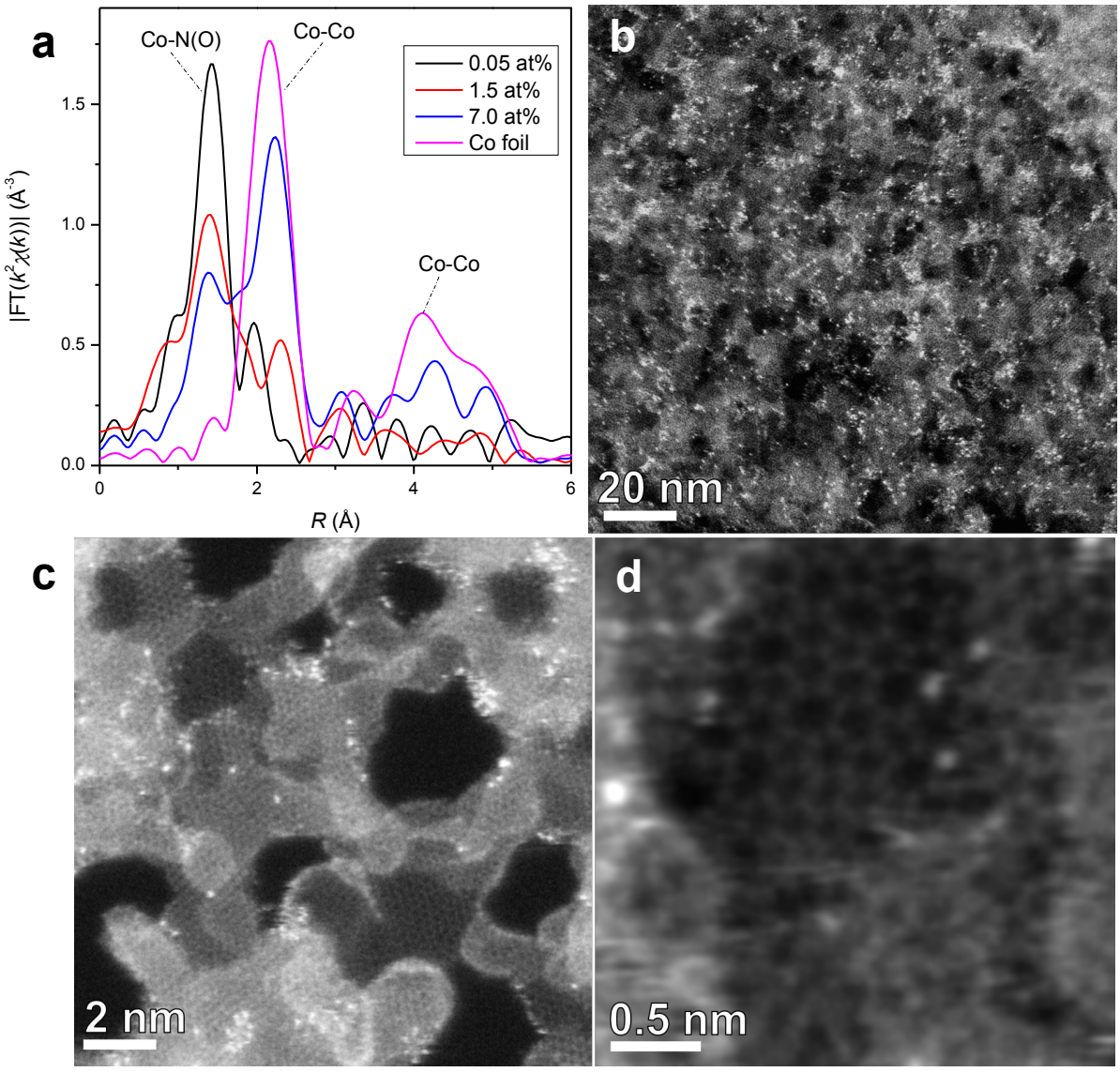

Figure 4.7. (a) EXAFS with different atomic percent of Co demonstrating the decrease of the Co-Co peak, and increase of the Co-N(O) peak. (b-d) HRTEM images of single atomic Co on the plane of graphene.

The synthesis of different single metal atoms was completed using a graphene oxide as a substrate. A very low concentration (0.05 %at) of the selected metal precursor was dispersed and mixed with graphene oxide. The metal precursor and graphene oxide solution was then hydrothermally treated to create a hydrogel. The hydrogel containing the metal will then be n-doped using high temperature annealing and ammonia gas. By n-doping the hydrogel, we created binding sites using the different nitrogen groups to bind to the single metal atoms.[29] Furthermore, using various metal precursors we synthesized different metal single atoms and test their ability as lithium-sulfur catalysts. However, more experiments will be completed in order to prove that we actually have single metal atoms. To do this, we will use a combination of EXAFS, XANES, DFT and TEM. The EXAFS seen in Figure 4.7a, is analysis of series of different Co at% in comparison to Co foil. At an R(A) of about 2.1, we see a strong Co-Co peak, suggesting Co-Co bonds. As we decrease the atomic concentration of the Co, the Co-Co peak decreases, and we see an increase of the peak at a R(A) of 1.5, which signifies the Co bond to N or O, and not another Co. Furthermore, we can use XANES to determine the oxidation state of the single metal atom, and perform a DFT study the to simulate how the metal atom is bound to the substrate. Finally, we can perform HRTEM to visibly see the single atoms as seen in Figure 4.7b-d**.** Using these techniques, we can prove that we successfully synthesized single metal atoms on our graphene substrate.

In order to characterize and compare different catalysts, three distinct piece of information was demonstrated. The cyclic voltammogram of the reduction and oxidation of lithium polysulfides contain three main peaks, two redox peaks, and one oxidation peak. Starting at 2.4 V and scanning negatively, the first redox peak of the CV at about 2.35 V is the initial reaction from high order polysulfides (Li_2S_8 & Li_2S_6) to low order polysulfides (Li_2S_4 & Li_2S_3).

Continuing to scan negatively, the next reduction peak at 2.10 V is the conversion from low order polysulfides to the final discharge product, Li_2S. Scanning in the positive direction, the large anodic peak at about 2.5 V is the conversion from polysulfide to sulfur. Using this information, we took the potential difference between the two main cathodic peaks and the main anodic peak, and compare them for each catalyst. The smaller the difference between the cathodic and anodic peaks, the lower the overpotential of the system, the better the performance of the catalyst. It is interesting to note that metals may effect the two reduction peaks differently. In Figure 4.8a, our study shows the CV of Mn, V, and Pt single atom catalysts compared to our n-doped graphene control. Interestingly, as seen in Figure 4.8b, each metal affects each redox peak in a different fashion. For example, Pt is the best at the oxidation at sulfur, where as Mn and V are each respectively best at the two redox peaks. This demonstrated to us that the initial reduction reaction to low order polysulfide, and the second reduction reaction to the final discharge product might require different metals catalysts to become fully optimized. Finally, we scanned each catalyst at increasing scan rates. By analyzing how the peak separation increases as we increase scan rate, we can determine how the catalyst would perform at higher current densities. This is demonstrated in Figure 4.8c-d using only graphene supports as an example. At 5 mV/s, regular graphene has a peak separation of 0.222 V, where as n-doped graphene has a peak separation of 0.145 V. As we increase the scan rate, at 100 mV/s graphene has a peak separation of 0.617 V where as n-doped graphene has a peak separation of 0.447 V. As the scan rate increase, the peak separation for the n-doped graphene, is less than regular graphene, thus it can be determined that n-doped graphene will be better at higher current densities. Using these analysis techniques, we effectively characterized and determine potential catalysts for lithium polysulfide redox reactions, however, more experiments still need to be completed.

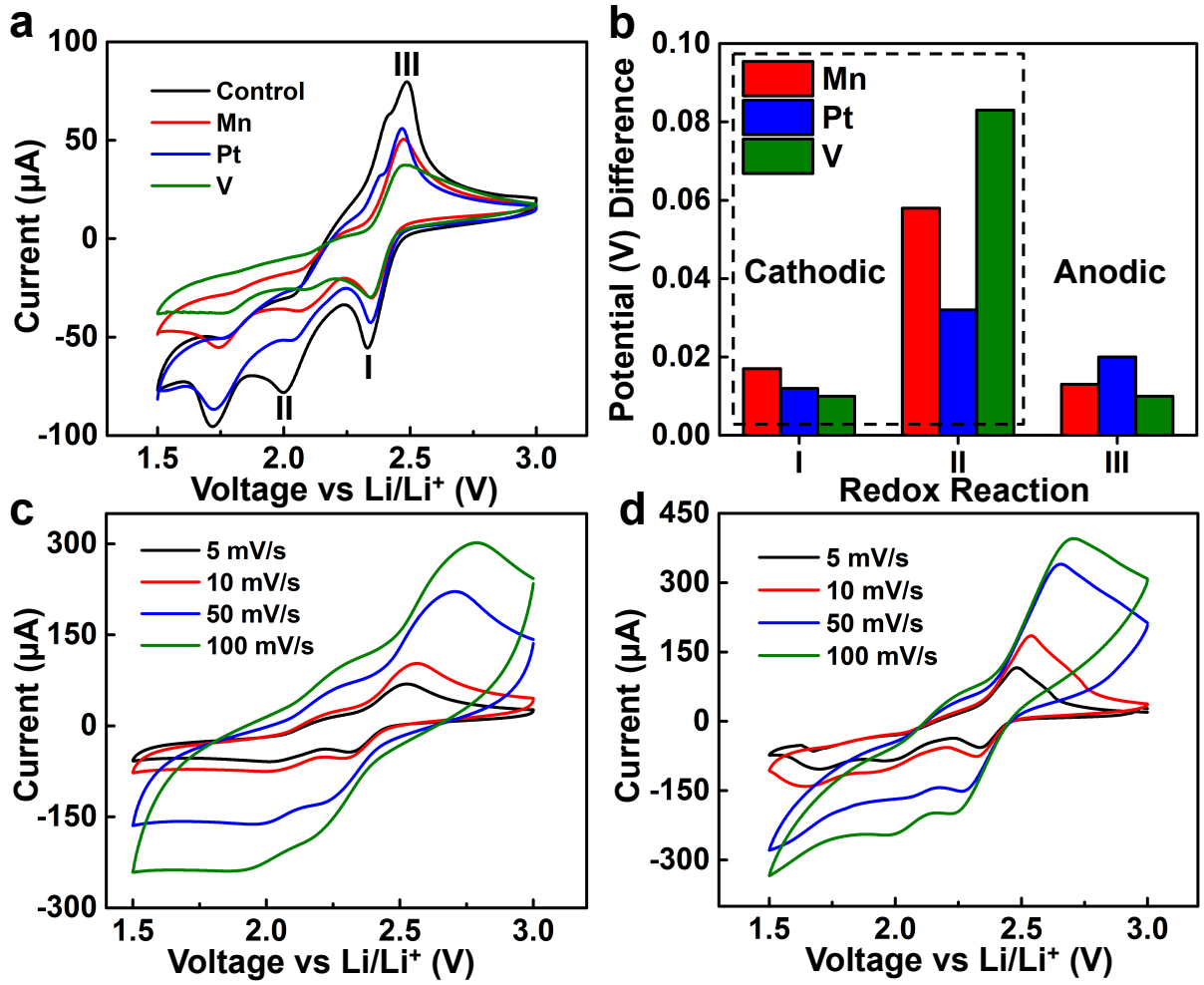

Figure 4.8. (a) Cyclic voltammetry of loaded single atom Mn, Pt, and V on an n-doped graphene support. (b) Comparison of the potential differences between the three metals in comparison to the n-doped graphene control. Different metals have different shifts at different redox peaks. I, II and III correspond to to their respective redox peaks in the Figure 4a. (c) Cyclic voltammetry of graphene at different scan rates. (d) Cyclic voltammetry of n-doped graphene at different scan rates.

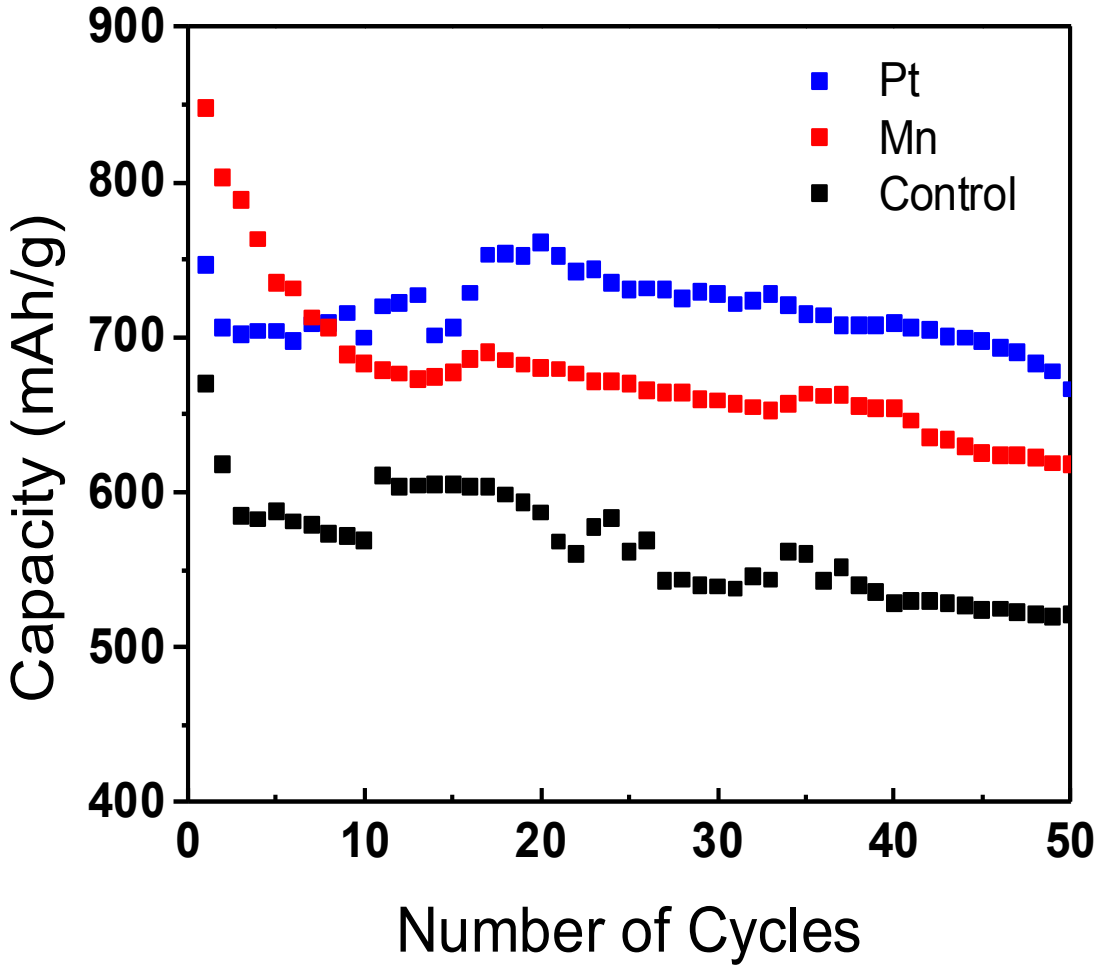

Figure 4.9. Galvanostatic cycling of single atom Pt, Mn, n-doped graphene control at 0.1 C.

Galvanostatic data was determined for the single atom Pt, Mn and the control n-doped graphene hydrogel as seen in Figure 4.9. At 0.1 C Mn has an initial capacity of 848 mAh g^{-1}, and after 50 cycles has a capacity of 662 mAh g^{-1}. Pt has a lower initial capacity of 745 mAh g^{-1}, however after 50 cycles has a higher capacity than the Mn electrode at 692 mAh g^{-1}. The n-doped graphene control has an initial capacity of 673 mAh g^{-1}, and after 50 cycles has a capacity

of 539 mAh g^{-1}. Both the Mn and Pt show superior capacity compared to the control, which can be attributed to the addition of the catalyst. To complete this study, cycling at higher rates has to be accomplished.

4.4 Conclusion

We demonstrated the usage of different catalysts for both a lithium-air, and lithium-sulfur system. We demonstrated the use of Pd_3Ni can be used as an effective catalyst for Li-Air Batteries. A Pd_3Ni/C cathode increases the cyclability of the battery by approximately 100% compared to just an activated carbon cathode, and it is able to cycle the approximately the same as just using a Pd Catalyst with 30% less Pd per particle. The Pd_3Ni/C cathode has also been shown to have a capacity of 5700 mAh g^{-1}, 30% higher than that of just a Carbon Black cathode. For lithium-sulfur batteries, we demonstrated the large improvement in capacity by using minimal amount of both Pt, and Mn atoms. We also demonstrate a potentiostatic screening technique that allows investigations of multiple different metals at a fast pace. Overall, the usage of a catalyst for energy storage applications with undergo a concerted reaction greatly benefits for the usage of a catalyst.

4.5 References

1. Girishkumar, G.; McCloskey, B.; Luntz, A. C.; Swanson, S.; Wilcke, W. Lithium-air battery: promise and challenges. *J. Phys. Chem. Lett.* **2010**, 1, 2193-2203.
2. Su, D., Kim, H.S., Kim, W.S., Wang, G. A study of Pt_xCo_y alloy nanoparticles as cathode catalysts for lithium-air batteries with improved catalytic activity. *J. of Power Sources*, **2013**, 244, 488-493.

3. Lu, Y.C., Xu Z., Gasteiger H.A.,Chen, S., Hamad-Schifferli K., Yang S.H. Platinum−Gold Nanoparticles: A Highly Active Bifunctional Electrocatalyst for Rechargeable Lithium−Air Batteries. *J. Am. Chem Soc*. **2010**, 132, 12170–12171

4. Lu Y.C., Gasteiger H.A., Yang S.H. Catalytic Activity Trends of Oxygen Reduction Reaction for Nonaqueous Li-Air Batteries. *J. Am. Chem. Soc*. **2011**, 133, 19048–19051

5. Gittleson F.S., Sekol R.C., Doubek, G., Linardib, M., Taylor A.D. Catalyst and electrolyte synergy in Li–O_2 batteries. *Phys. Chem. Chem. Phys*. **2014**, 16, 3230-3237.

6. Chen, L., Guo, H., Fujita, T., Hirata, A., Zhang, W., Inoue, A., Chen. M. Nanoporous PdNi Bimetallic Catalyst with Enhanced Electrocatalytic Performances for Electro-oxidation and Oxygen Reduction Reactions. *Adv. Funct. Mater.* **2011**, 21, 4364–4370.

7. Mizushima, K.; Jones, P.; Wiseman, P.; Goodenough, J. B. Li_xCoO_2 ($0<x\leq1$): a new cathode material for batteries of high energy density. *Mater. Res. Bull.* **1980**, *15*, 783-789.

8. Yamada, A.; Chung, S.-C.; Hinokuma, K. Optimized $LiFePO_4$ for lithium battery cathodes. *J. Electrochem. Soc.* **2001**, *148*, A224-A229.

9. Armand, M.; Tarascon, J.-M. Building better batteries. *Nature* **2008**, *451*, 652-657.

10. Tarascon, J.-M.; Armand, M. Issues and challenges facing rechargeable lithium batteries. *Nature* **2001**, *414*, 359-367.

11. Bruce, P. G.; Freunberger, S. A.; Hardwick, L. J.; Tarascon, J.-M. Li-O_2 and Li-S batteries with high energy storage. *Nat. Mater.* **2012**, *11*, 19-29.

12. Yang, Y.; Zheng, G.; Cui, Y. Nanostructured sulfur cathodes. *Chem. Soc. Rev.* **2013**, *42*, 3018-3032.

13. Ji, X.; Lee, K. T.; Nazar, L. F. A highly ordered nanostructured carbon-sulphur cathode for lithium-sulphur batteries. *Nat. Mater.* **2009**, *8*, 500-506.

14. He, G.; Ji, X.; Nazar, L. High "C" rate Li-S cathodes: sulfur imbibed bimodal porous carbons. *Energy Environ. Sci.* **2011**, *4*, 2878-2883.

15. Lin, T.; Tang, Y.; Wang, Y.; Bi, H.; Liu, Z.; Huang, F.; Xie, X.; Jiang, M. Scotch-tape-like exfoliation of graphite assisted with elemental sulfur and graphene–sulfur composites for high-performance lithium-sulfur batteries. *Energy Environ. Sci.* **2013**, *6*, 1283-1290.

16. Manthiram, A.; Fu, Y.; Chung, S.-H.; Zu, C.; Su, Y.-S. Rechargeable lithium-sulfur batteries. *Chem. Rev.* **2014**, *114*, 11751-11787.

17. Zhang, S. S. Liquid electrolyte lithium/sulfur battery: fundamental chemistry, problems, and solutions. *J. Power Sources* **2013**, *231*, 153-162.

18. Ji, X.; Nazar, L. F. Advances in Li-S batteries. *J. Mater. Chem.* **2010**, *20*, 9821-9826.

19. Zang, J.; An, T.; Dong, Y.; Fang, X.; Zheng, M.; Dong, Q.; Zheng, N. Hollow-in-hollow carbon spheres with hollow foam-like cores for lithium-sulfur batteries. *Nano Res.* **2015,** *8*, 2663-2675.

20. Zhang, K.; Zhao, Q.; Tao, Z.; Chen, J. Composite of sulfur impregnated in porous hollow carbon spheres as the cathode of Li-S batteries with high performance. *Nano Res.* **2013**, *6*, 38-46.

21. Qiu, Y.; Li, W.; Li, G.; Hou, Y.; Zhou, L.; Li, H.; Liu, M.; Ye, F.; Yang, X.; Zhang, Y. Polyaniline-modified cetyltrimethylammonium bromide-graphene oxide-sulfur nanocomposites with enhanced performance for lithium-sulfur batteries. *Nano Res.* **2014**, *7*, 1355-1363.

22. Seh, Z.; Li, W.; Cha, J.; Zheng, G.; Yang, Y.; McDowell, M.; Hsu, P.; Cui, Y. Sulfur-TiO_2 yolk-shell nanoacheticture with internal void space for long-cycle lithium-sulfur batteries. *Nature Comm.* **2013**, 4, 1331.

23. Pang, Q.; Kundu, D.; Cuisinier, M.; Nazar, L.F. Surface-enhanced redox chemistry of polysulfides on a metallic and polar host for lithium-sulfur batteries. *Nature Comm*. **2014**, 5,4759.

24. Su, Y.S., Manthiram, A. Lithium–sulphur batteries with a microporous carbon paper as a bifunctional interlayer. *Nature Comm*. **2012**, 3, 1116.

25. Salem, H.A., Babu, G., Rao, C.V., Arava, L.M.R. Elctrocatalytic Polysulfide traps for controlling redox shuttle process of Li-S batteries. *J. Am. Chem. Soc.* **2015**, 137, 11542–11545.

26. Wang, J.X., Markovic, N. M., Adzic, R. R. Kinetic Analysis of Oxygen Reduction on Pt(111) in Acid Solutions: Intrinsic Kinetic Parameters and Anion Adsorption Effects. *J. Phys. Chem. B*. **2004**, 108, 4127.

27. Xu, C.X., Zhang, Y., Wang, L.Q., Xu, L.Q., Bian, X.F., Ma, H.Y., Ding, Y. Nanotubular Mesoporous PdCu Bimetallic Electrocatalysts toward Oxygen Reduction Reaction. *Chem Mater*. **2009**, 21, 3110.

28. Abel, M., Robach, Y., Porte, L. Stress induced surface structures and reactivity of thin layer Pd/Cu(1 1 0) deposits. *Surf. Sci*. **2002**, 498, 244.

29. Fei, H., Dong, J., Arellano-Jimenez, M.J., Ye, G., Kim, N.D., Samuel, E.L.G., Peng, Z., Zhu, Z., Qin, F., Bao, J., Yacaman, M.J., Ajayan, P.M., Chen, D., Tour, J.M. Atomic cobalt on nitrogen-doped graphene for hydrogen generation. *Nature Communications*. **2015**, 8668.

Chapter 5

5.1 Conclusion

Exploring cathode materials that provide a higher capacity such as oxygen for lithium air batteries (3842 mAh g^{-1}), or sulfur for lithium-sulfur batteries (1675 mAh g^{-1}), will pave the way for the next generation of energy storage which is largely limited by the theoretical capacities of the cathode materials such as $LiCoO_2$ (272 mAh g^{-1}), and $LiFePO_4$ (170 mAh g^{-1}). In the first chapter, we discussed in detail about the problems of each material, for example, the many side reactions of lithium-air batteries, or the polysulfide shuttling of lithium-sulfur batteries, and explored possible solutions to these problems.

In the second chapter, we investigated the usage of a three-dimensional graphene membrane for a high energy density lithium-air battery in ambient condition. Using the hydrophobic tortuous three-dimensional graphene membrane we were able to inhibit the diffusion of water vapor and create a lithium-air battery that cycles over 2000 times with a capacity limited at 140 mAh g^{-1}, over 100 cycles with a capacity limited at 1425 mAh g^{-1}, and over 20 cycles at the high capacity of 5700 mAh g^{-1}, which is substantially better than Li-ion batteries today.

In the third chapter, we explored the usage of a three-dimensional graphene aerogel to maximize the loading of sulfur to create a freestanding electrode with high capacity for a lithium-sulfur batteries. We demonstrated that our three-dimensional graphene aerogel could sustain a loading of 95% by weight, and we achieved a capacity of 969 mAh g^{-1} normalized by the entire electrode with a 90% sulfur loading. We also showed how the three-dimensional graphene aerogel was able to combat the main issues with lithium-sulfur batteries.

Finally, in the fourth chapter, we examine the usage of different catalyst systems in both lithium-air and lithium-sulfur batteries. We probe into how different noble metal configurations are optimal for Li-Air batteries, specifically Pd_3Ni. We showcase how different metals effect the sulfur reduction reaction using potentiostatic methods, and inspect galvanostatically how both Pt and Mn increase the capacity of lithium-sulfur batteries by interacting with the sulfur redox reactions intermediate species, but further characterization needs to be carried out. Overall, my dissertation has explored the problems with next generation energy storage cathode materials, and provided possible solutions in order to bring us one step closer to brining these materials into commercialization.